

This is an Open Access document downloaded from ORCA, Cardiff University's institutional repository:<https://orca.cardiff.ac.uk/id/eprint/132119/>

This is the author's version of a work that was submitted to / accepted for publication.

Citation for final published version:

Davis, Timothy A. , Nguyen, Dieu D., Seth, Anil C., Greene, Jenny E., Nyland, Kristina, Barth, Aaron J., Bureau, Martin, Cappellari, Michele, den Brok, Mark, Iguchi, Satoru, Lelli, Federico, Liu, Lijie, Neumayer, Nadine, North, Eve V., Onishi, Kyoko, Sarzi, Marc, Smith, Mark D. and Williams, Thomas G. 2020. Revealing the intermediate-mass black hole at the heart of the dwarf galaxy NGC404 with sub-parsec resolution ALMA observations. *Monthly Notices of the Royal Astronomical Society* 496 (4) , pp. 4061-4078. 10.1093/mnras/staa1567

Publishers page: <http://dx.doi.org/10.1093/mnras/staa1567>

Please note:

Changes made as a result of publishing processes such as copy-editing, formatting and page numbers may not be reflected in this version. For the definitive version of this publication, please refer to the published source. You are advised to consult the publisher's version if you wish to cite this paper.

This version is being made available in accordance with publisher policies. See <http://orca.cf.ac.uk/policies.html> for usage policies. Copyright and moral rights for publications made available in ORCA are retained by the copyright holders.





# Revealing the intermediate-mass black hole at the heart of the dwarf galaxy NGC 404 with sub-parsec resolution ALMA observations

Timothy A. Davis<sup>1</sup>,<sup>\*</sup> Dieu D. Nguyen,<sup>2</sup> Anil C. Seth,<sup>3</sup> Jenny E. Greene,<sup>4</sup> Kristina Nyland,<sup>5</sup> Aaron J. Barth,<sup>6</sup> Martin Bureau,<sup>7,8</sup> Michele Cappellari,<sup>7</sup> Mark den Brok,<sup>9</sup> Satoru Iguchi,<sup>2,10</sup> Federico Lelli,<sup>1</sup> Lijie Liu,<sup>7</sup> Nadine Neumayer,<sup>11</sup> Eve V. North,<sup>1</sup> Kyoko Onishi,<sup>12</sup> Marc Sarzi,<sup>13</sup> Mark D. Smith<sup>7</sup> and Thomas G. Williams<sup>11</sup>

*Affiliations are listed at the end of the paper*

Accepted 2020 May 29. Received 2020 May 25; in original form 2020 April 1

## ABSTRACT

We estimate the mass of the intermediate-mass black hole at the heart of the dwarf elliptical galaxy NGC 404 using Atacama Large Millimetre/submillimetre Array (ALMA) observations of the molecular interstellar medium at an unprecedented linear resolution of  $\approx 0.5$  pc, in combination with existing stellar kinematic information. These ALMA observations reveal a central disc/torus of molecular gas clearly rotating around the black hole. This disc is surrounded by a morphologically and kinematically complex flocculent distribution of molecular clouds, that we resolve in detail. Continuum emission is detected from the central parts of NGC 404, likely arising from the Rayleigh–Jeans tail of emission from dust around the nucleus, and potentially from dusty massive star-forming clumps at discrete locations in the disc. Several dynamical measurements of the black hole mass in this system have been made in the past, but they do not agree. We show here that both the observed molecular gas and stellar kinematics independently require a  $\approx 5 \times 10^5 M_{\odot}$  black hole once we include the contribution of the molecular gas to the potential. Our best estimate comes from the high-resolution molecular gas kinematics, suggesting the black hole mass of this system is  $5.5_{-3.8}^{+4.1} \times 10^5 M_{\odot}$  (at the 99 per cent confidence level), in good agreement with our revised stellar kinematic measurement and broadly consistent with extrapolations from the black hole mass–velocity dispersion and black hole mass–bulge mass relations. This highlights the need to accurately determine the mass and distribution of each dynamically important component around intermediate-mass black holes when attempting to estimate their masses.

**Key words:** galaxies: dwarf–galaxies: elliptical and lenticular, cD–galaxies: evolution–galaxies: individual: NGC 404–galaxies: ISM–galaxies: kinematics and dynamics.

## 1 INTRODUCTION

Supermassive black holes (SMBHs) are ubiquitous at the centres of massive galaxies. Over the past few decades the masses of these SMBHs have been carefully measured using stellar and gas dynamical methods (see e.g. the review by Kormendy & Ho 2013). These measurements reveal that SMBH masses scale with many properties of their host galaxies. However, much less is known about the presence of black holes (BHs) in dwarf galaxies, let alone whether they obey the scaling relations observed at higher masses (e.g. Greene 2012).

Given the difficulty of growing SMBHs from stellar mass BHs (even when accreting for a Hubble time), it is thought that massive BHs must instead grow from more massive seeds (e.g. Madau & Rees 2001; Volonteri, Haardt & Madau 2003; Greene, Strader & Ho 2019; Inayoshi, Visbal & Haiman 2020). The exact processes that form these seeds, and the seeds’ intrinsic mass distribution, are currently unknown. Measurements of the masses of central

BHs in dwarf galaxies can constrain these important, but very poorly understood processes. While in massive galaxies the memory of the original BH has long since been erased, dwarf galaxies experience far less merging or accretion. The mass distribution, occupation fraction, and scaling relations of the intermediate-mass black holes (IMBHs) in dwarf galaxies today can thus help constrain seeding mechanisms (e.g. Volonteri 2012; Ricarte & Natarajan 2018).

Some dwarf galaxies with stellar masses  $\sim 10^9 M_{\odot}$  appear not to host a central BH. In the Local Group, Gebhardt et al. (2001) published an upper limit of just  $1500 M_{\odot}$  for the mass of a putative BH in the low-mass spiral galaxy M33, while in the dwarf elliptical galaxy NGC 205 any central BH has a mass below  $\sim 10^4 M_{\odot}$  (Valluri et al. 2005; Nguyen et al. 2019). The four closest dwarf galaxies outside the Local Group known to host a central BH are NGC 404, NGC 4395, NGC 5102, and NGC 5206 and all have published dynamical BH mass estimates (Seth et al. 2010; den Brok et al. 2015; Nguyen et al. 2017, 2018, 2019). However, weighing these BHs is at the edge of what is feasible with state-of-the-art adaptive optics observations. Thus, dynamical measurements of BH masses in dwarf galaxies (expected to have BH masses  $< 10^6 M_{\odot}$ )

\* E-mail: [DavisT@cardiff.ac.uk](mailto:DavisT@cardiff.ac.uk)

do not extend much beyond the Local Group, limiting detection of these BHs to the small subset of objects that are actively accreting (e.g. Greene, Ho & Barth 2008; Reines, Greene & Geha 2013; Miller et al. 2015).

In this paper we report on sub-parsec resolution Atacama Large Millimeter/submillimeter Array (ALMA) molecular gas observations of the dwarf elliptical galaxy NGC 404. This object has a total stellar mass of  $\approx 1.2 \times 10^9 M_{\odot}$  (Seth et al. 2010), hosts a large-scale low-surface brightness region of star formation (coincident with a large-scale H I ring) and a disc/ring of dust closer to its centre, both likely accreted during a recent (minor) merger (del Rfo, Brinks & Cepa 2004; Thilker et al. 2010). NGC 404 also hosts an accreting BH (see e.g. Nyland et al. 2017). Limits on the mass of this BH have been estimated (Seth et al. 2010; Nguyen et al. 2017) both from modelling of the stellar kinematics (yielding  $M_{\text{BH}} < 1.5 \times 10^5 M_{\odot}$ ), and using the kinematics of a rotating disc of hot ( $\approx 2300$  K) molecular hydrogen at its centre (suggesting  $M_{\text{BH}} < 2 \times 10^5 M_{\odot}$ ). The best-fitting measurements from these papers do not agree particularly well, perhaps because the hot-H<sub>2</sub> gas has significant non-circular motions. However, we also know that this object has a substantial mass of molecular gas at its centre ( $\approx 9 \times 10^6 M_{\odot}$ ; Taylor, Petitpas & del Rio 2015), that may contribute significantly to the galaxy potential and thus bias the existing BH mass measurements. Depending on the range of radii where the gas is dynamically important, this could lead to either an over- or underestimate of the BH mass. Here we probe the distribution of the cold CO(2-1) emitting molecular gas in NGC 404 at sub-parsec scales with ALMA. With these data (which reach higher spatial and spectral resolution than all previous observations) we not only obtain an independent estimate of the BH mass using the kinematics of the cold molecular material (e.g. Davis et al. 2013b), but can also improve our stellar kinematic estimates of the BH mass in this object.

In Section 2 we discuss the ALMA data this paper is based on. In Section 3 we incorporate the molecular gas distribution into our stellar kinematic models, and derive a new constraint on the BH mass of NGC 404. In Section 4 we model the kinematics of the molecular gas itself and obtain an independent estimate of the BH mass. We discuss our results in Section 5 before concluding in Section 6. We assume a distance of  $3.06 \pm 0.37$  Mpc to NGC 404 (derived using the tip of the red giant branch method; Karachentsev et al. 2002), yielding a physical scale of  $14.8 \text{ pc arcsec}^{-1}$ .

## 2 ALMA DATA

The <sup>12</sup>CO(2–1) line in NGC 404 was observed with an extended ALMA configuration twice on 2015 October 31, as part of programme 2015.1.00597.S. These data, which detected the central disc in this object, were presented in Nyland et al. (2017). In this work we include three additional ALMA tracks. The first, taken with extended baselines on 2015 September 5 did not pass initial quality assurance due to the lack of a suitable amplitude calibrator, but upon further inspection was found to be usable. Two additional lower resolution tracks were obtained on 2018 June 16 and September 3 as part of project 2017.1.00572.S.

In each of these observations an 1850 MHz correlator window was placed over the <sup>12</sup>CO(2–1) line, yielding a continuous velocity coverage of  $\approx 2000 \text{ km s}^{-1}$  with a raw channel width of  $\approx 0.6 \text{ km s}^{-1}$ , sufficient to properly cover and sample the line. Three additional 2 GHz-wide low-resolution correlator windows were simultaneously used to probe continuum emission.

The raw ALMA data were calibrated using manual calibration scripts in the Common Astronomy Software Applica-

tions (CASA) package. Phase and bandpass calibration were performed using the quasars J2253+1608, J0237+2848, J0112+3522, and J0112+3208, while flux calibration was performed using quasar J0238+1636.

We used the CASA package to combine and image the visibility files of the different tracks. For each of the data cubes discussed below, continuum emission was detected, and subtracted in the  $uv$ -plane using the CASA task UVCONTSUB. These continuum subtracted data were then imaged in order to produce a 3D RA-Dec-velocity data cube (with velocities determined with respect to the rest frequency of the <sup>12</sup>CO(2-1) line). This dirty cube was cleaned in regions of source emission (identified interactively) to a threshold equal to twice the root-mean square (RMS) noise of the dirty channels. Our source is very extended at the spatial resolution of our observations, and thus we used a multiscale clean algorithm (Rau & Cornwell 2011) with cleaning scales optimized for point sources, and emission with a characteristic scale 3, 6, and 9 times the synthesized beam. The clean components found from this analysis were then added back and reconvolved using a Gaussian beam of full-width-at-half-maximum (FWHM) equal to that of the dirty beam. The resulting cube was then corrected for the primary beam response.

In this work we make use of two different sets of CO(2-1) data products. The first high-resolution data set, which we use for our kinematic modelling, was produced from the three long baseline tracks only, imaged using Briggs weighting (robust parameter 0.5). This yields a synthesized beam of  $0.''051 \times 0.''026$  at a position angle of  $-10^{\circ}$  (a mean physical resolution of 0.54 pc) and an RMS noise of  $0.79 \text{ mJy beam}^{-1} \text{ channel}^{-1}$ . This data set allows us to image the central disc at the highest spatial resolution possible, but it does not recover all the flux. The second combined data set was produced from all available ALMA tracks, imaged using Briggs weighting (robust parameter 0.1). This yields a synthesized beam of  $0.''078 \times 0.''037$  at a position angle of  $21^{\circ}$  (a mean physical resolution of 0.8 pc), and an RMS noise of  $0.61 \text{ mJy beam}^{-1} \text{ channel}^{-1}$ . This combination allows us to retrieve almost all the flux from this object (see below), but at a slight penalty to spatial resolution. We use this data set when discussing the morphology of the gas. Both data sets use a channel width of  $2 \text{ km s}^{-1}$  and pixels of  $0.''015 \times 0.''015$ .

## 2.1 Line emission

We clearly detect CO(2-1) line emission in NGC 404. In our combined data set we find an integrated line flux of  $161 \pm 16 \text{ Jy km s}^{-1}$  within the inner  $8'' \times 8''$  ( $\approx 120 \text{ pc}^2$ ). This error is dominated by the  $\approx 10$  per cent flux calibration uncertainties. The high-resolution data set resolves out 74 per cent of this emission, which is why we only use it for kinematic modelling.

Taylor et al. (2015) presented a low-resolution map of CO(1-0) in this source, and combining their observed flux density with our own suggests a CO(2-1)/CO(1-0) ratio in beam temperature units of  $\approx 0.6$ , within the range found in normal spiral galaxies (e.g. Leroy et al. 2009). To check if we are likely to be resolving out flux even in our combined data set, we reduced the ALMA Compact Array (ACA) data available for this source from project 2017.1.00907.S. The gas in NGC 404 is barely resolved by the ACA, and this data should thus provide a good measurement of the total flux. We derive a total CO(2-1) flux of  $174 \pm 17 \text{ Jy km s}^{-1}$  from these data, in agreement with the estimate from our combined data set. This suggests that we are not resolving out significant flux in our combined data set, despite its extremely high spatial resolution.

Zeroth (integrated intensity), first (mean light-of-sight velocity), and second (line-of-sight velocity dispersion) moment maps of the

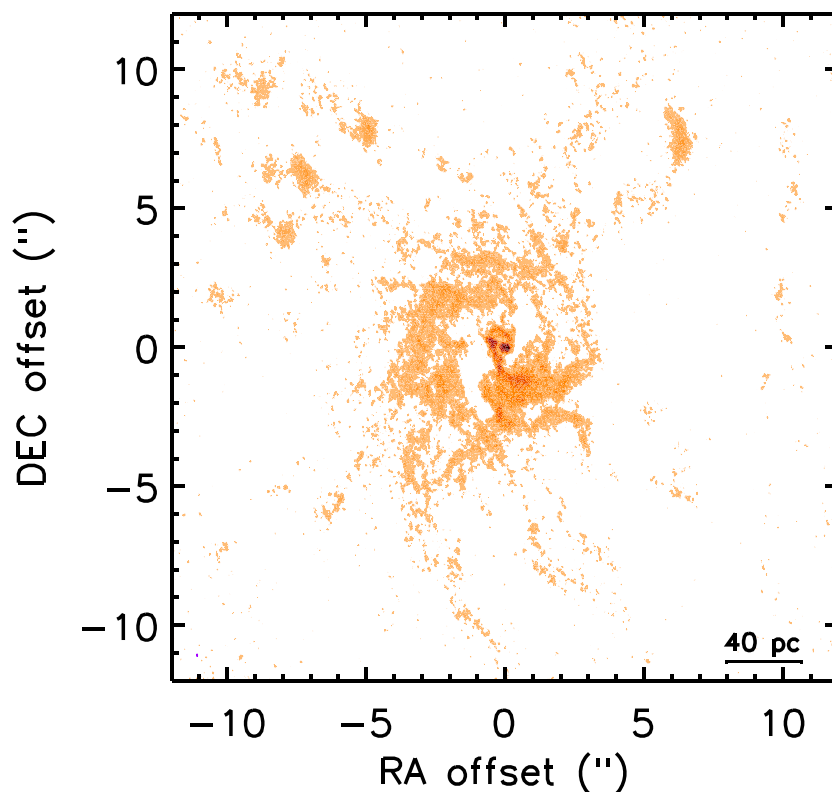


**Figure 1.** Zeroth moment (integrated intensity) map of the  $^{12}\text{CO}(2-1)$  emission in NGC 404, created from our combined data set using the masked-moment technique described in Section 2. The synthesized beam ( $0.''078 \times 0.''037$  or  $\approx 0.8 \text{ pc}^2$ ) is shown as an extremely small purple ellipse at the bottom left-hand corner of the figure. Our  $\approx 0.8 \text{ pc}$  resolution data reveal the complex morphology of the gas in the centre of this gas-rich dwarf elliptical galaxy.

detected line emission were created from the combined datacube using a masked moment technique (see Dame 2011). These moments are presented in Figs 1 and 2. Fig. 3 shows moment zero contours overplotted on *Hubble Space Telescope* (*HST*) images of the stellar light (in the F336W filter), and ionized gas ( $\text{H}\alpha + [\text{N II}]$ ) emission from *HST* narrow-band imaging) of NGC 404. These *HST* images were calibrated astrometrically by Nguyen et al. (2017) and the ALMA data are overlaid using their native astrometric solution based on the known position of the phase-calibrator sources. A major-axis position-velocity diagram (PVD) was extracted from the same data cube with a position angle of  $37^\circ$  (the best-fitting position angle determined for the central disc of molecular gas, see Section 4) and a width of 5 pixels and is shown in Fig. 4. Coordinates in these plots are shown relative to the phase centre of the ALMA data, International Celestial Reference System (ICRS) position  $01^{\text{h}}09^{\text{m}}27.^{\text{s}}001, +35^\circ 43' 04.''942$ .

The morphology of the molecular gas in NGC 404 is complex. A clearly rotating central disc/torus structure is present within the central  $\approx 5 \text{ pc}$ , at the same location as the hot- $\text{H}_2$  disc (Seth et al. 2010). A zoomed view of the central region of the galaxy, highlighting this disc, is shown in Fig. 5. The position of the apparent kinematic centre of this disc coincides with the peak of the spatially resolved nuclear radio continuum source (possibly associated with a confined jet; Nyland et al. 2017), suggesting the disc is rotating around the central accreting BH. It is the kinematics of this central material that we will concentrate on to determine the black hole mass (Section 4). The emission outside this region is dominated by a ring-like structure containing multiple highly resolved molecular clouds and filaments, that correspond to dust features seen in absorption in

the *HST* images (Fig. 3). The morphology and kinematics of these clouds will be discussed in detail in Section 5.1 and Liu et al. (in preparation).

## 2.2 Continuum emission

We imaged the continuum emission of NGC 404 at a mean frequency of 237 GHz using the line free region of all spectral windows from all observed tracks. We used a multiscale clean algorithm, as discussed above, and additionally tapered the data in the  $uv$ -plane (yielding a synthesized beam of  $0.''67 \times 0.''46$  or  $\approx 9.9 \times 6.8 \text{ pc}$ ) to maximize our sensitivity to diffuse, extended emission. The resulting continuum image has an RMS noise of  $17 \mu\text{Jy beam}^{-1}$ . Continuum emission was detected from four different positions in NGC 404. Fig. 6 shows the inner three sources as blue contours, overplotted on the CO(2-1) combined moment zero map. The final source is located well to the north, outside the CO(2-1) detection region. The centroid positions and integrated fluxes of these four emission regions are tabulated in Table 1. We return to the nature of these sources in Section 5.2.

## 3 STELLAR KINEMATIC MODELLING

Limits on the mass of the BH in NGC 404 were estimated in the past (Seth et al. 2010; Nguyen et al. 2017) using both stellar kinematics and gaseous tracers (hot- $\text{H}_2$  lines in the near-infrared). As discussed above, while the limits from these measurements overlap, the best-fitting BH masses do not agree, and it has been posited that this is because the hot- $\text{H}_2$  gas is kinematically disturbed. However, the previous kinematic measurements included a model of the stellar

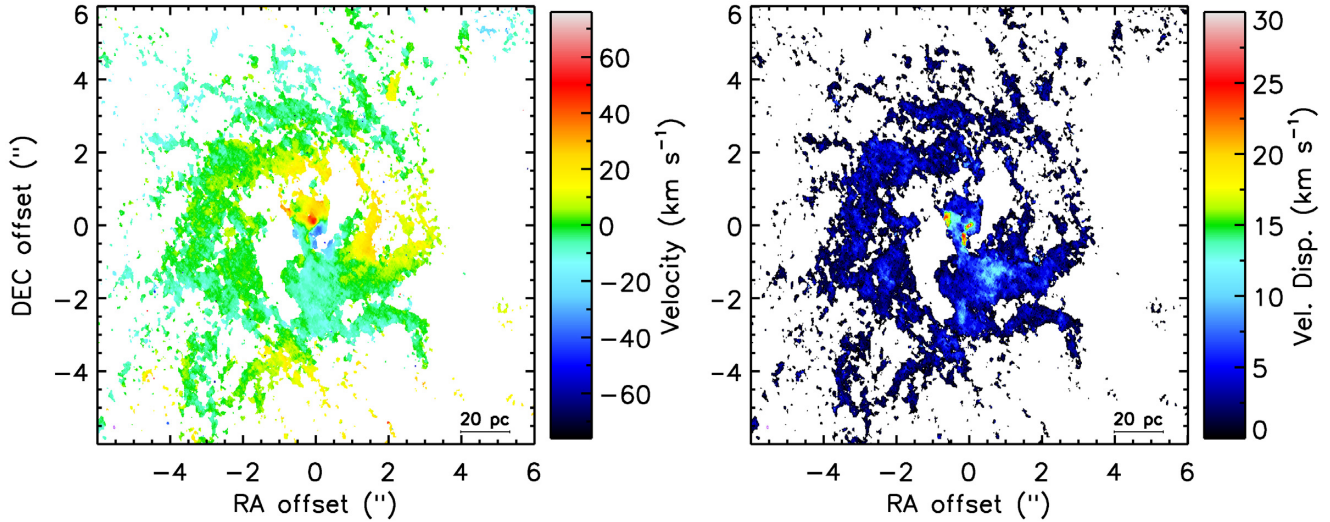


**Figure 2.** First and second moment (mean line-of-sight velocity and velocity dispersion) maps of the  $^{12}\text{CO}(2-1)$  emission in NGC 404, created from our combined data set using the masked-moment technique described in Section 2. The synthesized beam ( $0.''078 \times 0.''037$  or  $\approx 0.8 \text{ pc}^2$ ) is shown as an extremely small purple ellipse at the bottom left of each panel. In the left-hand panel, the velocity is shown relative to the systemic velocity of NGC 404, here assumed to be  $-53 \text{ km s}^{-1}$ . The gas in NGC 404 is rotating, at least in the centre, but becomes kinematically complex in the outer parts.

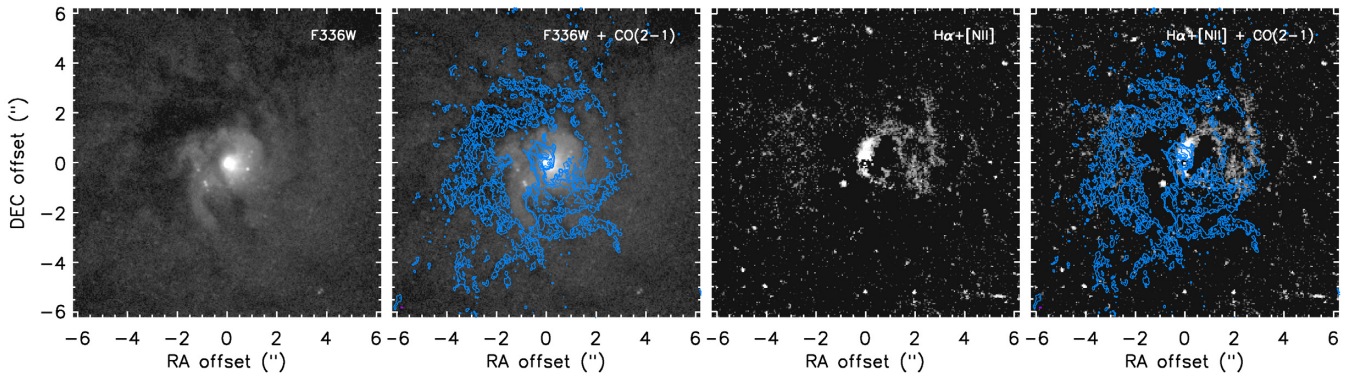


**Figure 3.** Left-hand panel: Unsharp-masked *HST* Wide Field Camera 3 (WFC3) F336W image of a  $180 \text{ pc} \times 180 \text{ pc}$  region around the nucleus of NGC 404, revealing a clear central dust disc/ring. Centre-left-hand panel: As before, but overlaid with blue  $^{12}\text{CO}(2-1)$  integrated intensity contours from our combined ALMA data set. The synthesized beam ( $0.''078 \times 0.''037$  or  $\approx 0.8 \text{ pc}^2$ ) is shown as a (very small) purple ellipse at the bottom left of the panel. The molecular gas disc coincides well with the dust structures seen in absorption. Centre-right-hand panel: Narrow-band *HST* image (F656N-F547M) of the  $\text{H}\alpha + [\text{NII}]$  lines in NGC 404. Right-hand panel: As before, but overlaid with blue  $^{12}\text{CO}(2-1)$  contours as in the central panel. Strong ionized-gas line emission is present in the centre and further out, where it fills some of the gaps in the molecular gas/dust ring.

mass in this object, but did not take into account the mass of the molecular gas component. As we show in Fig. 1, molecular gas is present in significant quantities in the vicinity of the BH in this object, and could thus affect measurements of the BH mass. If the gas were concentrated primarily around the BH then clearly this would lead to an overestimate of the BH mass (e.g. Medling et al. 2019), as the molecular gas mass would be wrongly ascribed to the central point mass. If, on the other hand, the gas were distributed more widely, but not following the stellar mass distribution, the stellar kinematic models would then be forced to assign a higher mass-to-light ratio to the stellar component to account for this unseen mass. In some cases this could cause the models to underestimate the BH mass.

To assess the impact of the molecular material on the stellar kinematic BH mass measurement in NGC 404 we re-run the stellar kinematic modelling procedure of Nguyen et al. (2017), now taking

into account the gravitational potential of the molecular gas. To do this we create a multi-Gaussian expansion (MGE; Emsellem et al. 1994; Cappellari 2002) model of the molecular material, using the python MGEFIT package to fit the molecular gas surface density map.<sup>1</sup> The resulting MGE is tabulated in Table 2. This model does not include the flocculent substructure of this system, but allows us to quantify the contribution to the potential of an ideal axisymmetric version of this observed molecular gas disc. We have assumed that the mass of any H I present around the nucleus of NGC 404 is negligible. This seems reasonable, given that the molecular gas in the centre of this object has a much higher surface density ( $\sim 10\,000 \text{ M}_{\odot} \text{ pc}^{-2}$ ) than usually found for H I (that typically saturates at  $\sim 10 \text{ M}_{\odot} \text{ pc}^{-2}$ ), and that H I observations of this object reveal a central hole (del

<sup>1</sup> Available from <https://pypi.org/project/mgefit/>

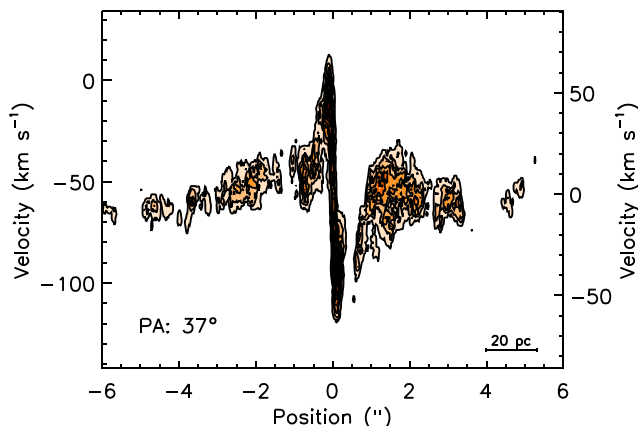


**Figure 4.** Position–velocity diagram of the  $^{12}\text{CO}(2-1)$  emission in NGC 404 from our combined data set, extracted along the kinematic major axis of the central disc-like emission ( $37^\circ$ ; see Section 4) with a slit of 5 pixels in width. We do not show the synthesized beam ( $0.''078 \times 0.''037$  or  $\approx 0.8 \text{ pc}^2$ ) or velocity channel width ( $2 \text{ km s}^{-1}$ ) explicitly in this plot, as they are very small compared to the ranges plotted. A clear signature of enhanced rotation is visible around the nuclear star cluster/putative IMBH, while the line-of-sight velocity of the gas is low in the outer parts, where the disc warps to become approximately face on.

Río et al. 2004). The mass of hot- $\text{H}_2$  emitting molecular gas in the nucleus of this galaxy is similarly not included, but as it has a total mass of  $< 1 M_\odot$  (Seth et al. 2010) it is dynamically unimportant. We are thus able to estimate the total gas mass from the molecular gas data alone, using the  $\text{CO}(2-1)/\text{CO}(1-0)$  ratio as calculated above and a Galactic  $\text{CO}$ -to- $\text{H}_2$  conversion factor of  $3 \times 10^{20} \text{ cm}^{-2} (\text{K km s}^{-1})^{-1}$  (Dickman, Snell & Schloerb 1986). We use a Galactic  $\text{CO}$ -to- $\text{H}_2$  conversion factor for NGC 404, as despite its low stellar mass it has approximately solar metallicity (Bresolin 2013). We discuss further the impact of this assumption in Section 4.5.

This model of the gas potential was then included with the stellar mass model of this system, along with an unknown BH mass. We use here the MGE model of the stellar mass distribution from Nguyen et al. (2017), constructed from *HST* images of the nucleus, using mass-to-light ratios calculated on a pixel-by-pixel basis from multiband colours (that should also correct for stellar population gradients and dust obscuration). We note that the lowest inclination allowed by this model of the stellar potential is  $16.^\circ 5$ . Using this combined mass model we performed a fit to the observed stellar kinematics using the Jeans anisotropic modelling (JAM) code of Cappellari (2008), relying on an axisymmetric solution of the Jeans equations incorporating orbital anisotropy. Full details of the fitting procedure can be found in Nguyen et al. (2017, 2019). The free parameters of this fit are the BH mass, orbital anisotropy, inclination of the system, and stellar mass normalization factor  $\Gamma$  (where  $\Gamma = 1$  corresponds to the mass derived from stellar population fitting in Nguyen et al. 2017 assuming a Chabrier 2003 initial mass function; IMF). These parameters were given flat priors (or flat in log space for the BH mass) and were allowed to vary within reasonable ranges (listed in Table 3).

Fig. 7 shows a visualization of the multidimensional parameter space explored by our fit to the stellar kinematic data. In the top panel of each column, a 1D histogram shows the marginalized posterior distribution of that given parameter, with the median and 68 per cent ( $1\sigma$ ) confidence interval indicated by vertical black dashed lines. In the panels below, the greyscale regions show the 2D marginalizations

of the fitted parameters, based on 3 million iterations. While the inclination of the system is at the lower bound allowed by the MGE model, the BH mass and stellar mass normalization factor  $\Gamma$  are well constrained (see Table 3). We find that the best-fitting BH mass of NGC 404 is  $5.1^{+3.9}_{-2.4} \times 10^5 M_\odot$  and the stellar mass normalization factor is  $\Gamma = 0.61 \pm 0.11$  (at the 68 per cent confidence level). This best-fitting JAM model is the median of the full posterior distribution, that has a reduced- $\chi^2$   $\chi_{\text{red}}^2 = 1.23$  over 920 degrees of freedom (Nguyen et al. 2017).

To better illustrate that our new JAM-stellar dynamical model fits the data with the aid of the additional molecular gas component, Fig. 8 shows the 1D radial profile of the RMS observed velocity ( $V_{\text{rms}}$ ) (as presented in Nguyen et al. 2017) versus our JAM predictions for axisymmetric mass models with different BH masses. While none of the models provide a perfect match to the data, BHs with  $M_{\text{BH}} \lesssim 10^5 M_\odot$  and  $\gtrsim 10^6 M_\odot$  are unable to fit the data from the inner parts of NGC 404 ( $R \lesssim 0.''5$  or  $7.4 \text{ pc}$ ).

This best-fitting BH mass is significantly higher than that previously derived from the same data, while the stellar mass normalization factor is significantly lower (Nguyen et al. 2017 found a  $3\sigma$  upper limit on the black hole mass of  $1.5 \times 10^5 M_\odot$  and  $\Gamma = 0.89^{+0.06}_{-0.05}$ ). This difference is not driven by the presence of molecular gas around the BH itself, but rather by the increasing contribution of molecular gas to the potential at larger radii ( $> 2 \text{ pc}$ ). We show this graphically in Fig. 9, plotting the cumulative mass within NGC 404 as a function of radius. The stellar and molecular gas contributions to the total mass budget are shown as red and blue solid lines, respectively. The stellar contribution has been estimated from our best-fitting JAM model parameters. The molecular gas contribution has been calculated in two independent ways, the first from our MGE model of the gas surface density (blue dashed line), the second from the clean components of the ALMA data (as discussed in Section 4.1; blue solid line). These estimates differ slightly but are very similar in shape and normalization. While the molecular material does not dominate the potential at any radius, it does provide a significant contribution towards the outer edge of the central molecular gas disc/torus (contributing 16 per cent of the luminous mass within  $0.''25$ ). At around 1 arcsec (the edge of the field of view of the Gemini data used to measure the stellar kinematics), this contribution grows to  $\approx 35$  per cent. The median contribution of the molecular gas within this field of view is 26 per cent. The contribution of the molecular gas to the gravitational potential peaks at 80 per cent at  $\approx 4$  arcsec in the large-scale molecular ring, before decreasing outside this. As shown by the red dashed line, if one were to ignore the presence of this molecular gas, then  $\Gamma = 0.89$  for the stellar component (as found by Nguyen et al. 2017) would match well the total mass profile. When one includes the potential of the molecular gas a much lower stellar mass normalization factor ( $\Gamma = 0.61$ ) is required. This lower stellar mass normalization decreases the amount of stellar mass present in the very central regions around the BH in our model, and thus a larger BH is required to fit the kinematics.

#### 4 MOLECULAR GAS KINEMATIC MODELLING

In the preceding section we used our extremely high-resolution map of the molecular gas in NGC 404 to include its contribution to the gravitational potential in our stellar kinematic modelling. This allowed us to obtain a new estimate of the BH mass in this low-mass galaxy. However, our ALMA observations can reveal more about the BH in this system. High-resolution molecular gas observations have been increasingly used in recent years to directly constrain BH masses (Davis et al. 2013b; Onishi et al. 2015; Barth et al. 2016a,b;

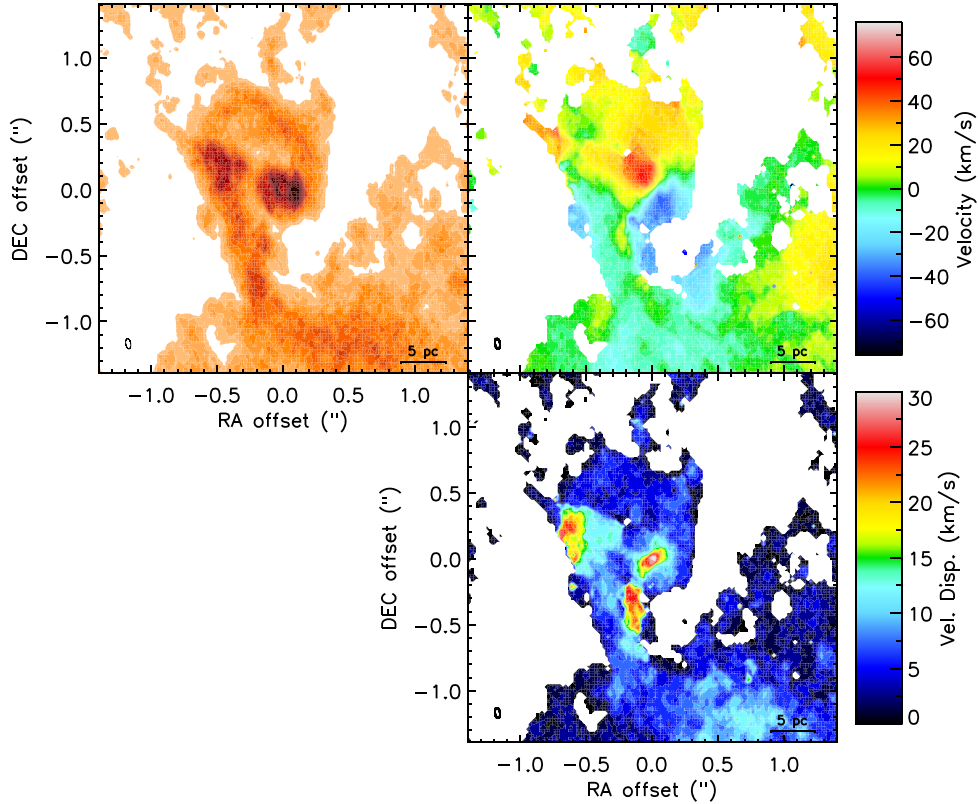


**Figure 5.** As for Figs 1 and 2, but for the central  $2.''8 \times 2.''8$  ( $\approx 42 \times 42$  pc) of NGC 404 only. The rotating gas in the central disc of NGC 404 can clearly be seen, along with a molecular gas one-armed spiral or arm connecting this disc to the ring present at large radii.

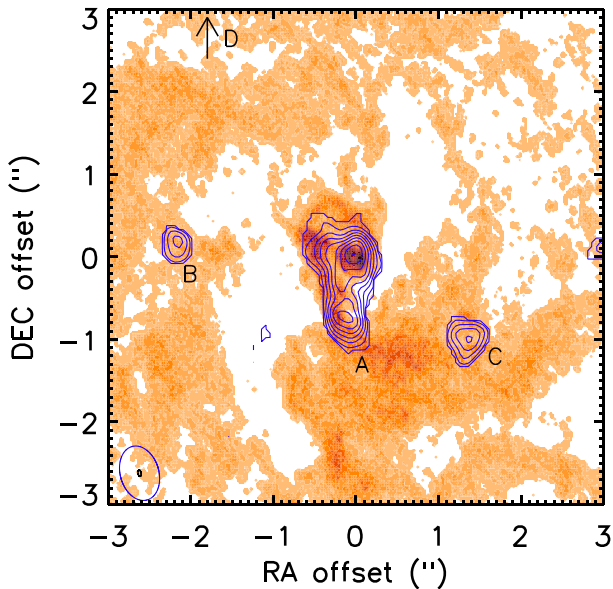


**Figure 6.** ALMA 237 GHz continuum emission (blue contours) overlaid on an integrated intensity map of the CO(2-1) emission in NGC 404 (orange). The continuum is imaged with a synthesized beam of  $0.''67 \times 0.''46$  (or  $\approx 9.9 \times 6.8$  pc) as shown in blue in the bottom-left-hand corner, while the  $0.''078 \times 0.''037$  (or  $\approx 0.8$  pc<sup>2</sup>) synthesized beam of the underlying CO(2-1) map is shown in black. An extended central continuum source is detected coincident with the molecular material, along with several point-like sources further out in the molecular ring. A fourth source is detected well outside the area shown in this figure.

Davis et al. 2017, 2018; Onishi et al. 2017; Boizelle et al. 2019; Combes et al. 2019; Nagai et al. 2019; North et al. 2019; Smith et al. 2019; Nguyen et al. 2020). In this section, we employ this technique to obtain an independent measurement of the mass of the IMBH in NGC 404.

To do this we concentrate on the molecular gas disc/torus within a radius of  $0.''25$  (or  $\approx 3.7$  pc) from the centre of NGC 404. We create a dynamical model of the molecular gas in this disc, including the gravitational influence of the stars and molecular gas along with that of the black hole. We use a forward modelling approach to compare the observed data cube with our model, and thus derive the best-fitting BH mass (and molecular gas disc parameters).

To achieve this we use the Kinematic Molecular Simulation (KINMS<sup>2</sup>) mm-wave observation simulation tool of Davis et al. (2013a), coupled to the Markov Chain Monte Carlo (MCMC) code KINMS\_MCMC<sup>3</sup>. This tool allows input guesses for the true gas distribution and kinematics and, assuming the gas is in circular rotation, produces a simulated data cube that can be compared to the observed data cube (taking into account the effects of beam-smearing, spatial and velocity binning, disc thickness, gas velocity dispersion, etc.). This tool has been applied to estimate BH masses in various other works (Davis et al. 2017, 2018; Onishi et al. 2017; North et al. 2019; Smith et al. 2019; Nguyen et al. 2020), each of which has iteratively improved the technique. We highlight the important aspects of this fitting procedure below.

<sup>2</sup><https://github.com/TimothyADavis/KinMS>

<sup>3</sup>[https://github.com/TimothyADavis/KinMS\\_MCMC](https://github.com/TimothyADavis/KinMS_MCMC)

**Table 1.** Continuum sources detected towards NGC 404 at 237 GHz.

| Description  | Label | RA<br>(hh:mm:ss.sss) | Dec<br>(°:':") | Ang. size    | Physical size<br>(pc <sup>2</sup> ) | Flux density<br>(mJy) |
|--------------|-------|----------------------|----------------|--------------|-------------------------------------|-----------------------|
| Centre + arm | A     | 01:09:26.999         | +35:43:05.02   | 1."55 × 0."9 | 23 × 13                             | 0.38 ± 0.02           |
| East         | B     | 01:09:27.175         | +35:43:05.17   | <0."7        | <10 × 10                            | 0.09 ± 0.02           |
| South-west   | C     | 01:09:26.886         | +35:43:03.93   | <0."7        | <10 × 10                            | 0.09 ± 0.02           |
| North        | D     | 01:09:27.133         | +35:43:14.81   | <0."7        | <10 × 10                            | 0.20 ± 0.02           |

**Table 2.** MGE fit to the molecular gas distribution in NGC 404.

| $\Sigma_{H_2}$<br>(M <sub>⊙</sub> pc <sup>-2</sup> ) | $\sigma$<br>(arcsec) | $q$  |
|--|----------------------|------|
| 13304.7  | 0.082                | 1.00 |
| 168.6  | 0.091                | 1.00 |
| 1409.4   | 0.380                | 1.00 |
| 975.9  | 2.187                | 1.00 |
| 38.2   | 4.492                | 1.00 |

*Note.* For each fitted component of the MGE, Column 1 lists its central molecular gas surface density, Column 2 its standard deviation (width), and Column 3 its axial ratio. All quantities are intrinsic (i.e. deconvolved).

**Table 3.** JAM model best-fitting parameters and statistical uncertainties.

| Parameters                            | Range       | Best fit | 1 $\sigma$ Error<br>(68 %) | 3 $\sigma$ Error<br>(99 %) |
|---------------------------------------|-------------|----------|----------------------------|----------------------------|
| (1)                                   | (2)         | (3)      | (4)                        | (5)                        |
| $\log_{10}(M_{\text{BH}}/M_{\odot})z$ | 2 → 7       | 5.71     | −0.28, +0.25               | −0.91, +0.59               |
| $\beta_z$                             | −1 → +1     | 0.48     | −0.10, +0.07               | −0.32, +0.18               |
| $i$ (°)                               | 16.5 → 90.0 | 16.73    | −0.09, +0.21               | −0.13, +0.60               |
| $\Gamma$                              | 0.1 → 1.7   | 0.61     | −0.11, +0.11               | −0.30, +0.30               |

*Note.* Columns 1 and 2 list the fitted model parameters, and their search ranges. The priors are uniform in linear space (except that of  $M_{\text{BH}}$  which is uniform in logarithmic space). Columns 3, 4, and 5 show the best-fitting value of each model parameter and its uncertainties at 1 $\sigma$  and 3 $\sigma$  confidence levels.

#### 4.1 Gas distribution

One of the inputs of KINMS is an arbitrarily parametrized gas surface brightness distribution. In most of the previous papers using this technique, an axisymmetric molecular gas distribution was assumed and fit to the data cube. As the molecular gas distribution in NGC 404 is clearly not axisymmetric we here utilize a different approach, making a model of the gas distribution based on the clean components generated when cleaning our observational data. This allows us to remove the uncertainty (and possible issues with model mismatch) caused by fitting the morphology of the gas distribution, as it is reproduced well by construction. We use the publicly available SKYSAMPLER<sup>4</sup> python code of Smith et al. (2019), that samples the observed clean components with an arbitrary number of point sources (10<sup>6</sup> in this case). These point sources have a uniform brightness, so more are generated in locations with bright molecular gas emission. These point sources can be deprojected at each step of our MCMC sampling algorithm to accurately reproduce the gas distribution observed at any proposed position angle and inclination.

Each point source can then be assigned a velocity based upon our kinematic model, described below.

#### 4.2 Mass model

The molecular gas in galaxies moves in response to the total gravitational potential of the galaxy, that includes the mass of both luminous (stars, gas) and dark (IMBH, dark matter) components. As above we use a mass model of NGC 404 to account for the contribution of luminous matter, and infer the mass of any dark object present. We include a BH in the model as a simple point mass at the kinematic centre of the galaxy.

To take into account the distribution of the stars in NGC 404, we again use the MGE model of the stellar mass distribution from Nguyen et al. (2017), as above. We fix the inclination used to deproject this mass distribution to that found in Section 3, although we note that the MGE model at the relevant radii is approximately spherical, so our results are insensitive to this choice. While in principle this model should already well describe the stellar mass, as before we include a mass normalization factor ( $\Gamma$ ) that can account for any systematic change in e.g the assumed IMF, star-formation, and chemical-enrichment histories of the stellar populations. In Section 3 we found  $\Gamma=0.61 \pm 0.11$  provides the best fit to the observed stellar kinematics. This mass normalization parameter is free in our molecular gas kinematic model, but we use this earlier determination as a prior to constrain our fit.

We note that this model does not formally include dark matter, as it is expected to be dynamically unimportant in the inner few parsecs of this galaxy, given its relatively high stellar surface density (e.g. Lelli et al. 2016). If dark matter were significant, its effect would simply be subsumed into the mass normalization factor (unless it has a density distribution markedly different from that of the stars).

In most massive galaxies, the stellar mass completely dominates. In NGC 404, however, we have shown above (Fig. 9) that the mass of the molecular material also matters, so we include it when calculating the circular velocity of the system. The molecular gas gravitational potential is calculated from a symmetrized version of our SKYSAMPLER cloudlets, assuming they lie in a thin but warped disc (we discuss the impact of this thin disc assumption in Section 4.5). The potential arising from this gas distribution is calculated using the Interactive Data Language (IDL) POTENTIAL\_NEWTON routine,<sup>5</sup> taking into account its full 3D distribution, and assuming each cloudlet has an equal fraction of the total gas mass. Within a radius of  $\approx 0."25$  (3.7 pc) from the centre of NGC 404 (the region included in our kinematic model) the total molecular gas mass is  $(2.5 \pm 0.3) \times 10^5 M_{\odot}$  (where the uncertainty in this quantity is dominated by the flux calibration). We note that if instead of using this cloudlet based method we had used the MGE model of the molecular gas potential derived in Section 3, our results would not have changed (see also Fig. 9).

<sup>4</sup><https://github.com/Mark-D-Smith/KinMS-skySampler>

<sup>5</sup>From Jeremy Bailin's IDL Utilities <http://simulated-galaxies.ua.edu/jbiu/>

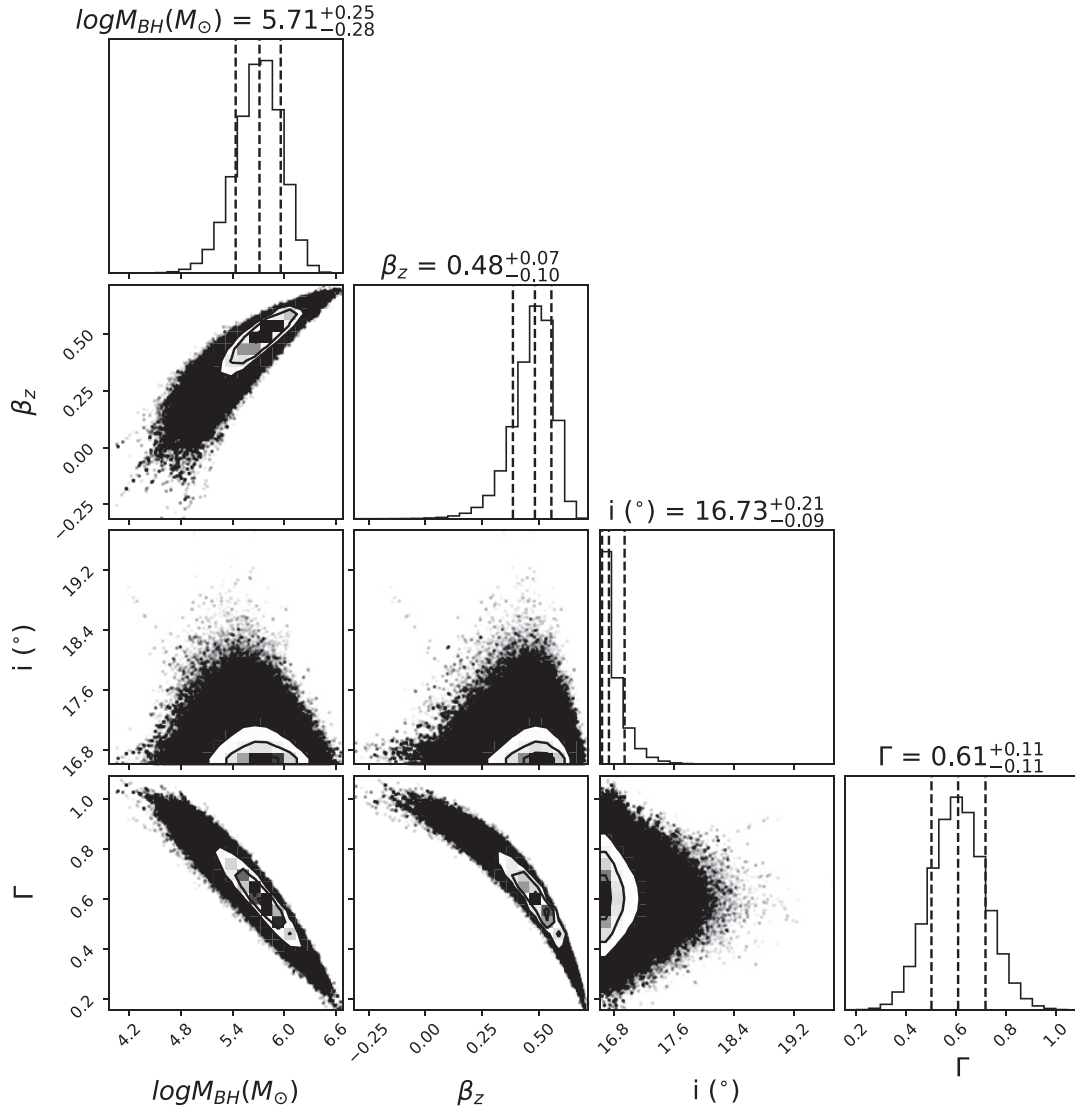


**Figure 7.** Multidimensional parameter space posterior distributions calculated for our JAM stellar-dynamical model of NGC 404. Top panels in the diagonal are marginalized 1D histograms, each showing the distribution of the corresponding column parameter. The median value and 68 per cent ( $1\sigma$ ) confidence levels are indicated with black dashed vertical lines. In the panels below, the three contours show the 2D marginalizations of the fitted parameters at the  $1\sigma$ ,  $2\sigma$ , and  $3\sigma$  confidence levels.

### 4.3 Gas kinematics

As Fig. 2 shows, the position angle and inclination of the gas disc in NGC 404 are clearly not radially constant (as also discussed by other authors, e.g. del R o et al. 2004), although they do seem approximately fixed inside the very compact molecular gas disc/torus. We thus fit the data in the central  $\approx 3$  pc of this source assuming a thin disc with radially constant but free inclination/position angle. Outside of this radius, where the molecular gas is concentrated in an arm-like feature, the gas distribution warps, continuously changing both its inclination and position angle (PA) with radius, before become flat again in the molecular (pseudo-)ring ( $R \gtrsim 15$  pc). Fitting our large-scale data following the procedure outlined below yields  $i = 9.3^\circ$  and  $\text{PA} = 1^\circ$  for the outer parts of this object, in agreement with the values derived by del R o et al. (2004) for the (even larger scale) H I ring. The simple model that we adopt thus includes the following features (listed as a function of radius); a flat disc of radially constant but free inclination and PA

within the inner 3 pc, a warped component between 3 and 15 pc (where the inclination and PA change linearly with radius), and a further un-warped disc at  $>15$  pc with parameters fixed to those found above ( $i = 9.3^\circ$  and  $\text{PA} = 1^\circ$ ). We note that in order to estimate the BH mass in this system we confine our kinematic model to galactocentric radii  $\leq 0.25''$  ( $\approx 3.7$  pc), and as such the warped material has very little effect on the fit. Using a simple single un-warped disc model does not result in a significant change in any of the derived parameters, although it does slightly increase their uncertainties.

We also include a parameter for the internal velocity dispersion of the gas, that is assumed to be spatially constant. We note that our treatment of the velocity dispersion is not fully self-consistent (i.e. we do not solve Jeans' equations but simply add a Gaussian scatter to our velocities). Given the low velocity dispersion in molecular gas clouds this is not expected to significantly influence our results, but we discuss this issue further in Section 4.5.

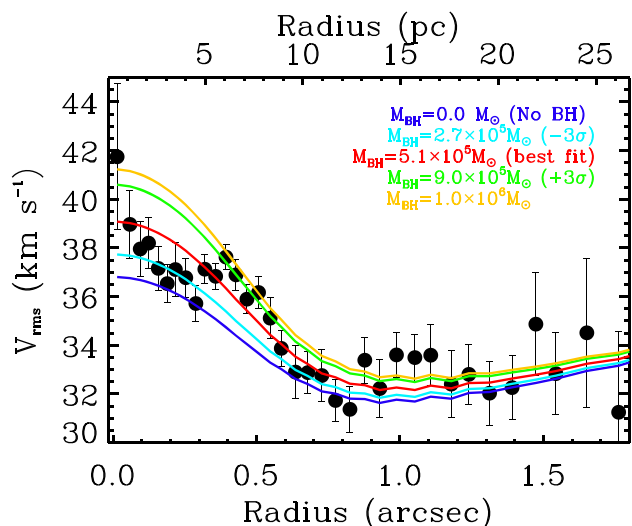


**Figure 8.** 1D radial profile of the RMS velocity  $V_{\text{rms}}$  versus our JAM prediction for axisymmetric mass models with different BH masses as listed in the legend. All models are fixed to the best-fitting anisotropy parameter ( $\beta_z = 0.5$ ), mass scaling factor ( $\Gamma = 0.61$ ), and inclination angle ( $i = 16.7^\circ$ ). The data are binned radially in bins of width 0.05 arcsec (or 0.7 pc). Our best-fitting model clearly favours an IMBH of mass  $(2.7\text{--}9.0) \times 10^5 M_\odot$ .

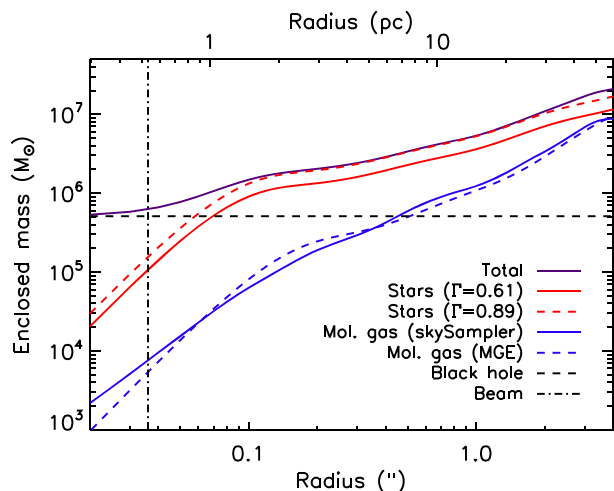


**Figure 9.** Enclosed mass of NGC 404 as a function of radius from our kinematic modelling (purple solid line). The contribution to the total mass from stars (with our best fitting  $\Gamma = 0.61$ ) is plotted as the red solid line, that from molecular gas as the blue lines (where the solid blue line shows the estimate from our SKYSAMPLER model, and the dashed blue line our MGE model estimate) and that from the black hole as the black dashed line. The red dashed line shows the stellar contribution with  $\Gamma = 0.89$  (as found by Nguyen et al. 2017), that would provide a good fit to the total mass enclosed if one did not know about the presence of molecular gas (that contributes significantly to the enclosed mass, especially at larger radii).

In this work we assume that the molecular gas is in circular motion, and hence that the gas rotation velocity varies only radially. Warps like that discussed above are likely to induce some non-circular motions, that could affect our dynamical measurements. We do not expect this to be important in the (apparently) un-warped central molecular gas torus/disc around the BH, but we can search for such signatures using the residuals around our best-fitting model (see Section 4.5).

#### 4.4 Bayesian analysis

As mentioned above, we use a Bayesian analysis technique to identify the best model and estimate uncertainties. This allows us to obtain samples drawn from the posterior distributions of each model parameter. Each parameter has a prior, that we typically set as a box-car over a reasonable parameter range (an assumption of maximal ignorance). The prior on the black hole mass is flat in log-space, with the mass allowed to vary between  $\log_{10}(\frac{M_{\text{BH}}}{M_\odot}) = 4.0$  and 6.9. For the mass normalization factor ( $\Gamma$ ) we use a Gaussian prior based on the measurement from Section 3. We constrain the inclination angle with a Gaussian prior around the best fit found in previous work,  $i = 37 \pm 3^\circ$  (Nguyen et al. 2017). The kinematic centre of the galaxy is constrained to lie within  $\pm 1$  arcsec of the optical galaxy centre position. The systemic velocity is allowed to vary by  $\pm 20 \text{ km s}^{-1}$  from that found by optical analyses. Details of all the priors are listed in Table 4.

Our MCMC procedure generates a model data cube and compares it to our observed data using a simple log-likelihood ( $\mathcal{L}$ ):

$$\mathcal{L}(a) = \frac{-\chi^2}{2} + \ln \left( \prod_{i=0}^n P(a_i) \right), \quad (1)$$

where  $\chi^2$  is the classical  $\chi^2$  statistic,  $P(a_i)$  is the prior probability of free parameter  $a_i$ , and  $n$  is the number of free-parameters in the fit.

As discussed in detail in Smith et al. (2019), because our ALMA data are noisy, the  $\chi^2$  statistic has an additional uncertainty associated with it, following the chi-squared distribution (Andrae 2010). This distribution has a variance of  $2(N - I)$ , where  $N$  is the number of constraints and  $I$  the number of inferred parameters. For our data  $N = 12112$ , so the variance becomes  $\approx 2N$ . Systematic effects can produce variations of  $\chi^2$  of the order of its variance (van den Bosch & van de Ven 2009), and ignoring this effect yields unrealistically small uncertainties. To mitigate this effect van den Bosch & van de Ven (2009) proposed to increase the  $1\sigma$  confidence interval to  $\Delta\chi^2 = \sqrt{2N}$ . To achieve the same effect within our Bayesian MCMC approach we need to scale the log-likelihood, as done by Mitzkus, Cappellari & Walcher (2017). This is achieved here by increasing the input errors (i.e. the assumed noise in the cube) by  $(2N)^{1/4}$  (in our case, with  $N = 12112$ , this equates to increasing the RMS by a factor of 12.47). This approach appears to yield physically credible formal uncertainties in the inferred parameters, whereas otherwise these uncertainties are unrealistically small. This correction does not account for the correlations between spaxels induced by the beam of the interferometer. These correlations can be accounted for using a covariance matrix (as in e.g. Davis et al. 2017), but this is computationally intensive and the effect is small compared to the variance correction applied above. Hence we neglect it here.

We utilize an MCMC method with Gibbs sampling and adaptive stepping to explore the parameter space. The algorithm runs until convergence is achieved, and then the best chain is run (with a fixed step size) for 300,000 steps (with a 10 per cent burn-in) to produce our final posterior probability distribution. For each model parameter the probability surfaces are then marginalized over to produce a best-fitting value (the median of the marginalized posterior samples) and associated 68 per cent and 99 per cent confidence levels (CLs). Fig. 10 shows the 1D and 2D marginalizations of the free parameters included in the fit. Quantitative descriptions of the likelihoods of all parameters are presented in Table 4. Most of our parameters are independent of each other, but we do find some degeneracies. As expected, the IMBH mass is degenerate with the mass-normalization

**Table 4.** Best-fitting model parameters and statistical uncertainties.

| Parameter<br>(1)  |       | Prior<br>(2)                   |      | Best fit<br>(3) | $1\sigma$ error (68 %)<br>(4) | $3\sigma$ error (99 %)<br>(5) |
|---|-------|--------------------------------|------|-----------------|-------------------------------|-------------------------------|
| Galaxy parameters:  |       |                                |      |                 |                               |                               |
| IMBH mass ( $\log_{10} M_{\text{BH}}/M_{\odot}$ )         | 4.0   | $\xrightarrow{\text{uniform}}$ | 6.9  | 5.74            | $-0.07, +0.11$                | $-0.51, +0.24$                |
| Mass normalization factor ( $\Gamma$ )                    |       | $N(\mu=0.61, \sigma=0.11)$     |      | 0.66            | $-0.07, +0.05$                | $-0.19, +0.16$                |
| Inclination ( $^{\circ}$ )                                |       | $N(\mu=37, \sigma=3)$          |      | 37.1            | $-0.46, +0.57$                | $-1.76, +1.61$                |
| Position angle ( $^{\circ}$ )                             | 10    | $\xrightarrow{\text{uniform}}$ | 70   | 37.2            | $-2.9, +2.4$                  | $-8.30, +7.81$                |
| Gas velocity dispersion ( $\sigma$ ; $\text{km s}^{-1}$ ) | 0.0   | $\xrightarrow{\text{uniform}}$ | 20.0 | 12.9            | $-\pm 0.9$                    | $-2.7, +3.6$                  |
| Nuisance parameters:                                      |       |                                |      |                 |                               |                               |
| Centre X offset (arcsec)                                  | -1.0  | $\xrightarrow{\text{uniform}}$ | 1.0  | 0.0             | $\pm 0.01$                    | $\pm 0.02$                    |
| Centre Y offset (arcsec)                                  | -1.0  | $\xrightarrow{\text{uniform}}$ | 1.0  | 0.0             | $\pm 0.01$                    | $\pm 0.02$                    |
| Centre velocity offset ( $\text{km s}^{-1}$ )             | -20.0 | $\xrightarrow{\text{uniform}}$ | 20.0 | -0.5            | $-1.2, +1.5$                  | $-3.8, +4.1$                  |

*Note.* Column 1 lists the fitted model parameters, while Column 2 lists the prior for each.  $N(\mu, \sigma)$  indicates a Gaussian prior with a given mean ( $\mu$ ) and standard deviation ( $\sigma$ ). Where the prior is listed as uniform, this is uniform in linear space (or in logarithmic space for the IMBH mass only). The posterior distribution of each parameter is quantified in the third to fifth columns (see also Fig. 3). The X, Y, and velocity offset nuisance parameters are defined relative to the International Celestial Reference System (ICRS) position  $01^{\text{h}}09^{\text{m}}27.^{\text{s}}001, +35^{\circ}43'04.''942$ , and the systemic (barycentric) velocity of the galaxy  $V_{\text{bary}} = -53 \text{ km s}^{-1}$ .

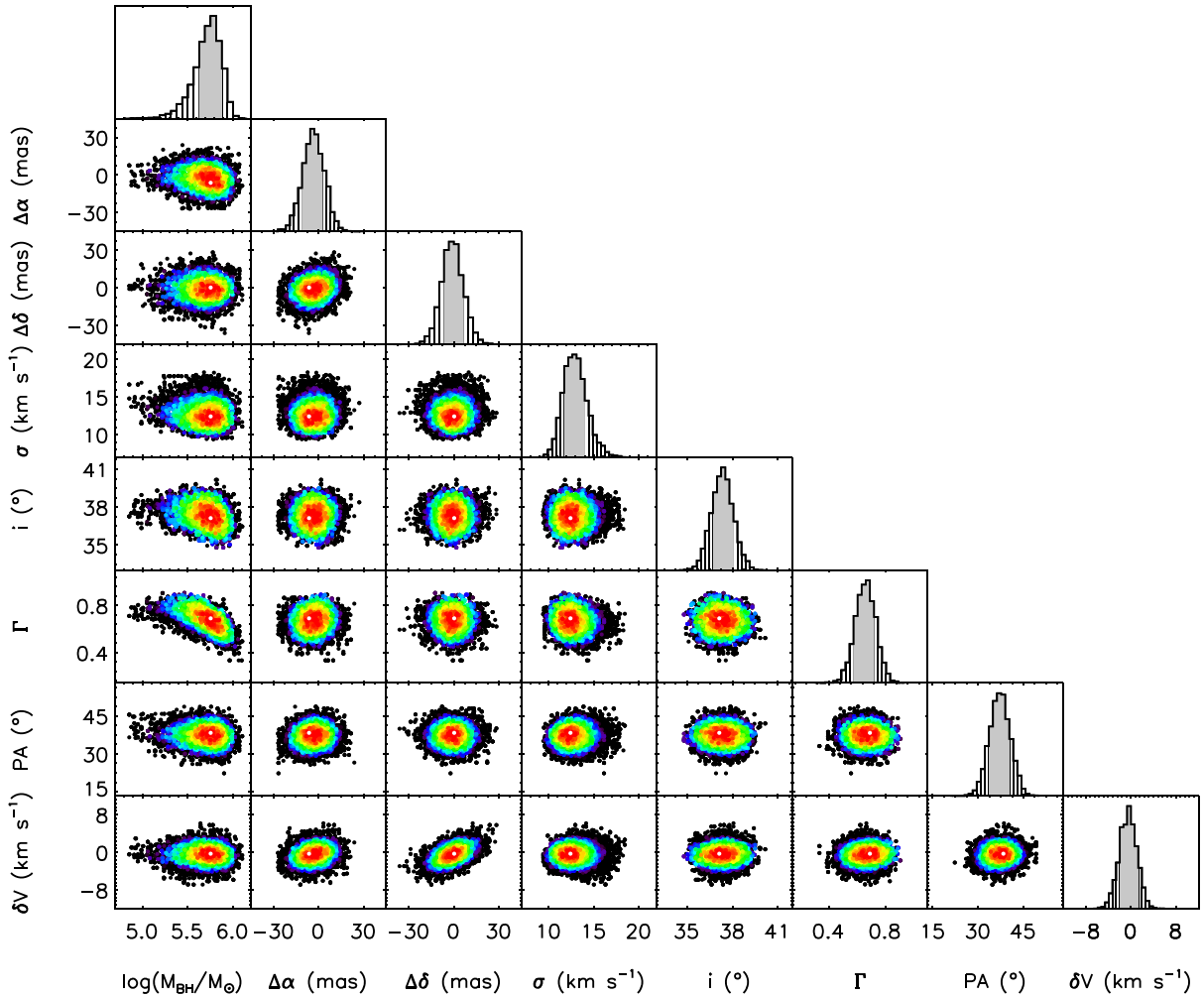


**Figure 10.** Visualization of the multidimensional parameter space explored by our molecular gas kinematic fit to the observed data of NGC 404 within galactocentric radii  $\leq 0.''25$  ( $\approx 3.7$  pc). In the top panel of each column a 1D histogram shows the marginalized posterior distribution of that given parameter, with the 68 per cent ( $1\sigma$ ) confidence interval shaded in pale grey. In the panels below, the coloured regions show the 2D marginalizations of those fitted parameters. Each point is a realization of our model, colour-coded to show the relative log-likelihood of that realization, with white points the most likely. The black points have  $\Delta\chi^2$  values outside the 99 per cent confidence interval. See Table 4 for a quantitative description of the likelihoods of all fitting parameters.

factor  $\Gamma$  and the inclination (as is always the case in any BH mass fit). The nuisance parameters (the kinematic centre of the galaxy within the cube) are also slightly correlated. Despite these degeneracies almost all these parameters remain constrained by these molecular gas data alone, and any additional scatter introduced is included when marginalizing to obtain our final uncertainties.

We clearly detect the presence of a dark object in the centre of NGC 404, with a mass of  $5.5_{-3.8}^{+4.1} \times 10^5 M_{\odot}$  (at the 99 per cent CL). Our best-fitting model provides a good fit to the data, as shown by Figs 11 and 12 that respectively show position–velocity diagrams and velocity fields extracted from our best-fitting model and compared with the observed data. As shown by Fig. 11, a model without an IMBH cannot provide a good fit to our data, nor can a BH of mass  $\gtrsim 10^6 M_{\odot}$ . Fig. 12 shows that the best-fitting model reproduces the observed velocity field well, leaving only low-level velocity residuals that are not spatially correlated.

#### 4.5 Uncertainties

In this section we briefly touch upon the main uncertainties that could affect the IMBH mass derived in this work.

First, given that we do not resolve the Keplerian increase of the circular velocity around the BH (see Fig. 11), our mass measurement is crucially dependent on the stellar mass model and its mass normalization factor ( $\Gamma$ ), that together with the molecular gas itself set the contribution of luminous matter to the observed gas kinematics. This model was constructed from multiband *HST* images, and carefully fitted pixel-by-pixel by Nguyen et al. (2017) to correct for stellar population gradients and dust obscuration. The mass normalization factor used here is that which provided the best fit to the stellar kinematics in Section 3 (and we incorporate the uncertainty of this measurement into our prior). Despite this, if the model were to be substantially biased, it would clearly have an effect on our derived BH mass. For instance, we can completely remove the need for an IMBH in NGC 404 if  $\Gamma > 1.15$ . Using the molecular gas data alone with a flat prior on  $\Gamma$  shows that, while possible, such a value is not the most likely with  $\Delta\chi^2 \approx 5$  (implying it deviates from the best fit by  $\gtrsim 2\sigma$ ). This same  $\Gamma$  would, however, be a  $4.3\sigma$  deviation from that found using stellar kinematics. The combination of these two data sets is thus crucial to allow us to accurately constrain the BH mass in NGC 404.

Secondly, the velocity dispersion (and the resulting vertical extension of the gas disc/torus) provides several additional sources of uncertainty. The first of these arises because we have assumed that the velocity dispersion is constant as a function of radius. If instead the velocity dispersion were to change substantially, it could bias our best-fitting BH mass. To test this we re-ran our best-fitting model, allowing for a linear gradient in velocity dispersion. The best-fitting velocity dispersion gradient was consistent with zero, suggesting that a constant velocity dispersion within the nuclear molecular gas disc is reasonable. In addition, our models do not take into account the additional dynamical support of the molecular gas due to its velocity dispersion. Due to the relatively low total rotation velocity ( $V$ ) of NGC 404, this ‘asymmetric drift’ correction is likely to be more important than in other systems with molecular gas BH mass measurements. We estimate the magnitude of this effect using the formalism described in Section 6.5 of Coccatto et al. (2006). We assume that the random motions in the gas disc are nearly equal in the radial ( $\sigma_r$ ) and vertical ( $\sigma_z$ ) directions, while the ratio of the velocity dispersion in the radial and azimuthal directions ( $\sigma_r/\sigma_{\phi}$ ) can be calculated under the epicyclic approximation, which is valid as long as  $\sigma_r \ll V$ . In our best-fitting model  $|V|$  is always  $>58 \text{ km s}^{-1}$

in the central disc of NGC 404 (the presence of the IMBH prevents the velocity decreasing further), and thus  $V/\sigma \gtrsim 5$  everywhere. This method can thus at least provide an approximate treatment of the asymmetric drift. Given these assumptions, we can use equation (12) of Coccatto et al. (2006) to calculate the asymmetric drift correction, that is then  $< 5$  per cent everywhere within the central disc of NGC 404. We thus conclude that asymmetric drift uncertainties are small compared to the other error sources, even in this low-mass object.

A related uncertainty arises from the assumption that the molecular material in the disc/torus of this object is distributed in a geometrically thin disc. If this material were instead to be geometrically thick this could bias the BH mass we estimate. To investigate this possibility we ran a further fitting procedure where the thickness of the disc was allowed to vary. Specifically the density as a function of height above the disc falls off following a Gaussian distribution, with the scale-height (the standard deviation of the Gaussian) left as a free parameter. A full description of this process is given in Appendix A. Assuming the molecular gas disc/torus in the central parts of this object is geometrically thick does not change the best-fitting BH mass in a statistically significant way (i.e the best-fitting BH mass is consistent with that found in Section 4.4 within the uncertainties). We are, however, able to set a  $1\sigma$  limit to the Gaussian scale-height in the vertical direction of  $z_h < 1.3 \text{ pc}$ , and thus a limit to the geometric thickness of this molecular disc/torus at its outer edge ( $r=0.25$  or  $3.7 \text{ pc}$ ) of  $z_h/r < 0.35$ . This result is consistent with simple theoretical expectations (see Appendix A). As such we conclude that the geometric thickness of the molecular disc/torus at the centre of NGC 404 is small, and not significantly biasing our derived BH mass.

Thirdly, we assume that the molecular gas in the central disc of NGC 404 is moving on circular orbits. This assumption is violated in the  $\approx 2300 \text{ K}$  molecular gas probed by  $\text{H}_2$  ro-vibrational lines (Seth et al. 2010; Nguyen et al. 2017), but we do not find evidence of significant non-circular motions in the cold gas from our ALMA observations. Our best-fitting model with purely circular motions provides a good fit to the data, as shown in Fig. 12. The residuals around the best fit have a low amplitude and no obvious spatial structure. Any low level non-circular motions that may be present are thus unlikely to have significantly affected our BH measurement.

Fourthly, as shown above, we know that the molecular gas mass contributes non-negligibly to the total mass of NGC 404 at the radii we study, and thus our BH mass estimate depends on the assumed CO-to- $\text{H}_2$  conversion factor ( $\alpha_{\text{CO}}$ ). Here we have assumed the molecular gas has a standard, Galactic  $\alpha_{\text{CO}}$ . This is motivated by the high metallicity of this object ( $\approx 0.8 Z_{\odot}$  in its outer parts, and thus presumably more metal rich in its centre; Bresolin 2013). However, if the true  $\alpha_{\text{CO}}$  of NGC 404 were to be significantly different, or vary radially, it could bias our BH mass estimate. Luckily, however, the two methods to estimate the BH mass we use here (stellar and gas kinematics) respond quite differently to the presence of the molecular gas mass. Our molecular gas kinematic analysis assumes the material moves in circular orbits, and thus the motion of any given parcel of gas is primarily sensitive to (and primarily constrain) the mass enclosed within its orbit. Given that the majority of the molecular material is located at large radii, this makes our molecular gas measurement fairly insensitive to  $\alpha_{\text{CO}}$  (the molecular gas in the central disc is essentially a massless kinematic tracer). Indeed, allowing  $\alpha_{\text{CO}}$  to vary over a large range ( $0.1 < \alpha_{\text{CO}} < 10 M_{\odot} (\text{K km s}^{-1} \text{ pc}^2)^{-1}$ ) in our fitting procedure does not significantly affect the best-fitting BH mass. The stellar kinematic modelling, on the other hand, is conducted over a large field of view (and stellar orbits explore a larger range of

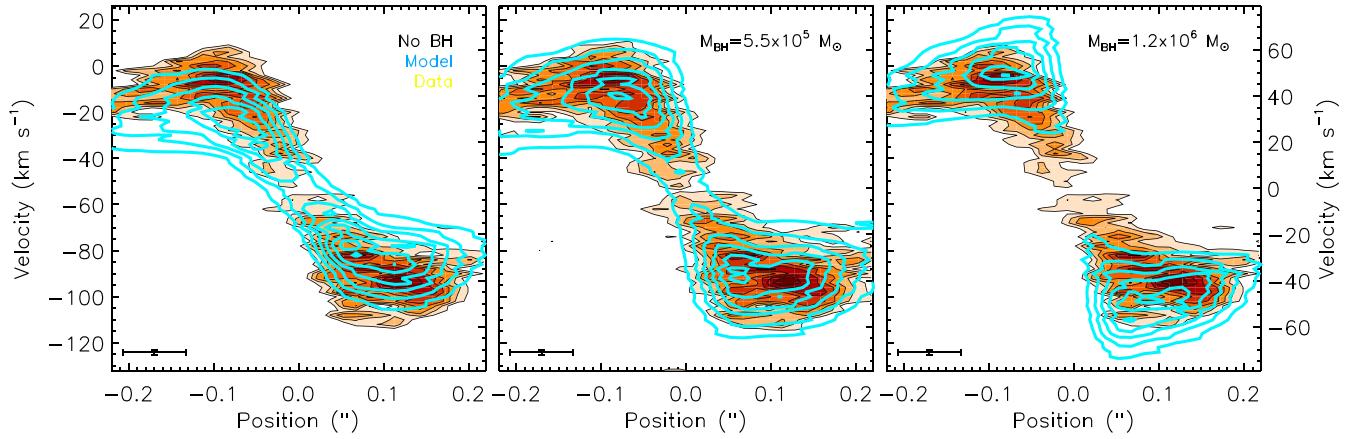


**Figure 11.** Position–velocity diagram extracted from the observed NGC 404 data cube (orange), overplotted with position-velocity data taken from our KINMS models (blue contours). Our spatial and velocity resolutions are shown as an error bar in the bottom-left corner of each plot. The central panel shows our best-fitting model with a  $5.5 \times 10^5 M_{\odot}$  IMBH, while the left-hand and right-hand panels show the same model with no BH, and with an SMBH ( $M_{\text{BH}} = 1.2 \times 10^6 M_{\odot}$ ), respectively. Clearly our best-fitting model provides a much better fit to the data.

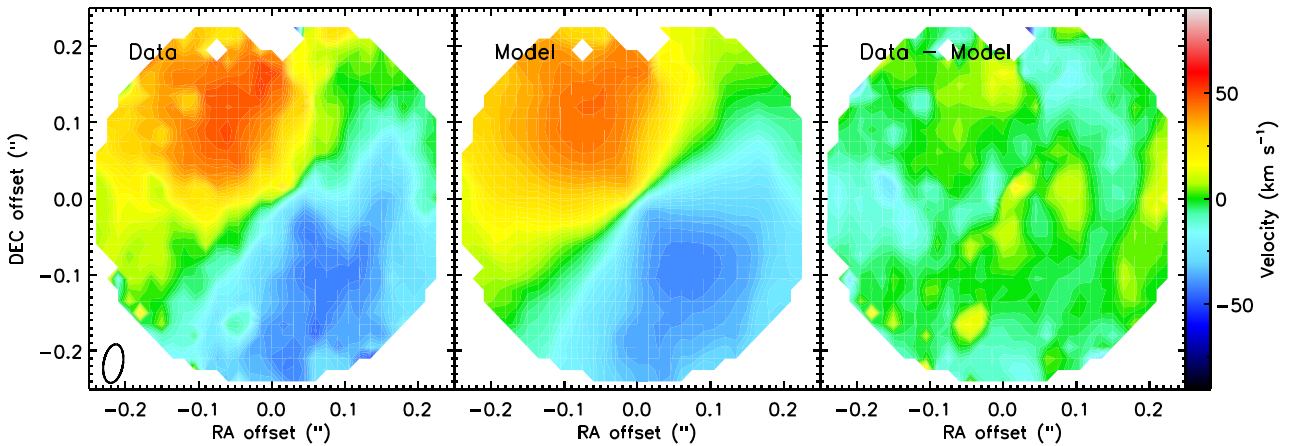


**Figure 12.** Left-hand and centre panels: Moment one maps of the CO(2-1) emission of the central disc ( $<0.''25$  or  $\approx 3.7$  pc) of NGC 404, extracted from our observed data cube (left-hand panel) and best-fitting model data cube (central panel). The synthesized beam ( $0.''051 \times 0.''026$  or  $0.54 \text{ pc}^2$ ) is shown in the bottom-left-hand corner of the left-hand panel. Right-hand panel: Residuals between the data and best-fitting model. The residuals are small (with a standard deviation of  $\approx 7 \text{ km s}^{-1}$ ) and do not show any obvious spatial correlation, suggesting our fit is good and no significant non-circular motion is present in the cold molecular gas disc.

radii), making it much more sensitive to the assumed  $\alpha_{\text{CO}}$ . Allowing a changing  $\alpha_{\text{CO}}$  in that analysis alters the derived BH mass by an order of magnitude. The fact that the two analyses agree well on the central BH mass when using a Galactic  $\alpha_{\text{CO}}$  thus suggests that this is a reasonable assumption for NGC 404.

Finally, all BH mass estimates are systematically affected by the distance ( $D$ ) they assume to their target galaxy (with  $M_{\text{BH}} \propto D$ ). For NGC 404 we use a tip of the red giant branch distance from Karachentsev et al. (2002), that has an uncertainty of 12 per cent. Here then, as with all other BH mass measurements, the distance-related systematic uncertainty on the BH mass is significant.

## 5 DISCUSSION

### 5.1 Gas morphology

The morphology of the molecular gas in NGC 404 is complex. As discussed in detail above, a central disc/torus of CO(2-1) emission is present, which peaks at a radius of about  $0.''16$  (2.3 pc), and

extends out to  $0.''25$  (3.7 pc). The disc itself is rotating around the IMBH, but is surrounded by kinematically distinct lopsided emission that appears connected to an arm-like feature. This arm joins to an incomplete (pseudo)-ring of emission, with a radius of  $\approx 2.''7$  (40 pc), that corresponds well to dust features identified in absorption against the stellar continuum in Fig. 3. Scattered molecular clouds exist beyond this radius, whose filamentary distribution mirrors that seen in H I at much larger radii (del Río et al. 2004).

The  $\text{H}\alpha + [\text{N II}]$  emission detected by *HST* anticorrelates with the presence of molecular gas (right-hand panel of Fig. 3), appearing to fill in many of the missing portions of this molecular (pseudo)-ring. This may be due to extinction in the dense molecular gas preventing detection of optical line emission where they are coincident, to star-formation feedback dissociating/removing gas in some parts of the ring, or to temporal stochasticity in the star-formation process at these small spatial scales.

Interestingly the Milky Way’s central molecular zone (CMZ) also hosts a lopsided ‘ring’ of molecular emission with star formation concentrated on one side (e.g. Molinari et al. 2011). NGC 404 could

thus host an interesting analogue to the CMZ that we are able to study face on. We do note, however, that some of the  $H\alpha$  near the centre of NGC 404 may be due to an ionization cone around the active galactic nucleus (AGN; Nyland et al. 2017) or a recent supernova remnant (Boehle et al. 2018). Disentangling the true mechanism ionizing the gas would require high spatial resolution observations of other nebula lines and is beyond the scope of this work.

The kinematics of the arm and ring features outside of the nuclear disc are complex. As shown in the first moment map in Fig. 2, the kinematic position angle appears to significantly change at radii  $>0.''7$  ( $>10$  pc), and the red/blue-shifts of the individual molecular clouds detected around the ring do not vary smoothly with position. This may be because we are seeing a truly chaotic distribution of clouds that do not lie in a settled disc. Alternatively, this outer material could be significantly more face-on than the disc around the galaxy nucleus (i.e. an inclination warp is present, as suggested by our kinematic modelling in Section 4), and thus the line-of-sight velocities we measure could be dominated by out-of-plane motions. The dynamical time at a radius of  $\approx 2.''7$  (40 pc), where the incomplete (pseudo)-ring of emission lies, is  $\approx 5.8$  Myr so in a flattened axisymmetric potential the warped disc we observe would be expected to relax quickly. The fact that we observe it suggests again that the potential of NGC 404 is approximately spherical at these radii.

The arm-like feature that extends between the outer (pseudo)-ring and the central disc of molecular emission appears to link the two, and it may be funnelling gas from the outer regions inwards (potentially fuelling the AGN). Our maps provide evidence that the arm hosts strong streaming motions, as the second moment (shown in Figs 2 and 5) reveals large line-widths along it. The fact that this arm-like feature is not symmetric could be because gas inflow is mainly stochastic, or it may point to a recent disturbance in the system.

The properties of the individual molecular clouds observed here will be discussed further in a future work (Liu et al., in preparation).

## 5.2 Continuum emission

As discussed above, and shown in Fig. 6, we detect spatially resolved 1 mm (237 GHz) continuum emission from the centre of NGC 404, and some additional point sources.

The central resolved source (labelled A in Fig. 6) is coincident with the molecular gas disc and arm at the core of NGC 404. Given its morphology, tracing the one-armed spiral connecting the central molecular disc to the (pseudo)-ring at larger radii, we consider it unlikely that this emission is from a background source. This emission was not detected in the previous ALMA observations presented in Nyland et al. (2017); it may have been resolved out. This feature has two distinct flux density maxima, one around the nucleus of the galaxy (coincident with the small radio jet identified over a range of radio frequencies; e.g. Nyland et al. 2017) and one at the base of the one-armed spiral feature. We note that this central source is detected in a higher resolution naturally weighted continuum map made without  $uv$ -tapering from our combined data set (at a resolution of  $0.''15 \times 0.''13$ ). At this resolution only the brightest areas around the nucleus, and the feature around the base of the arm are detected.

Various physical mechanisms could be causing this extended continuum emission. The centrally concentrated flux around the black hole overlaps with hot dust emission ( $\approx 950$  K) observed in the near-infrared (Seth et al. 2010; Dumont et al. 2020), the extended  $H\alpha$  source visible in Fig. 3, and the small radio jet. We consider it likely that the majority of this emission is from the Rayleigh–Jeans tail of

the dust continuum, as its flux is far higher than the pure-synchrotron extrapolation of the jet spectral energy distribution (Nyland et al. 2017), but we cannot rule out the presence of a very flat-spectrum radio core.

The second continuum maximum at the base of the molecular ‘arm’ could again contain contributions from several possible physical mechanisms. This is a location where one might expect shock heating to be important, as the gas flows inward along this arm towards the centre. Indeed, Fig. 2 shows an elevated molecular gas velocity dispersion along this feature.  $C$ - or  $J$ -shocks in the molecular medium can lead to continuum emission, and if the material flowing into the shock moves fast enough, or is very dense, the predicted continuum flux density can match that found for this source (e.g. McKee & Hollenbach 1987). Such shocks should, however, be even brighter at 15 GHz, but this feature was not detected in the  $Ku$ -band data of Nyland et al. (2017). We thus conclude that this extended continuum feature is again likely dominated by dust continuum emission, with possible small contributions from synchrotron in the jet region and hydrodynamic shocks along the arm.

Three other continuum sources are significantly detected in our continuum image. One (labelled B in Fig. 6) lies to the east, overlapping with a  $\approx 1.''3$  (20 pc) long molecular filament, while another (labelled C in Fig. 6) lies to the south-west, at the base of a filamentary spur of molecular emission. The final source (labelled D in Fig. 6) is located well to the north, away from the regions with detected molecular gas. Once again, it is not clear what powers the emission in these sources. They are associated neither with radio emission at 15 GHz, nor significant  $H\alpha$  emission. While  $H\alpha$  emission can easily be hidden due to dust, the lack of radio emission suggests that the emission is not free-free from H II regions nor synchrotron from supernova remnants.

Another possibility is that these three sources are the most extreme star-forming clumps/cores in NGC 404, that stand out from the diffuse dust background that may be resolved out. If their continuum luminosities are due to Rayleigh–Jeans emission from dust, then assuming a temperature of 50 K and a canonical gas-to-dust ratio of 100, we find that the total masses of the clumps would be at least  $6 \times 10^4 M_\odot$ , making them similar to the most massive clumps/cores in the Milky Way (Urquhart et al. 2018). Additional continuum data at higher frequencies would be required to confirm this hypothesis.

The remaining possibility is that some/all of these continuum sources are background galaxies. Based on the model of Cai et al. (2013), and given our sensitivity, we would expect to detect  $\approx 3$ – $4$  high- $z$  sources in our primary beam at  $3\sigma$  significance. As such, this is a viable explanation of these emission features, but the fact that 3/4 of these sources are clustered in the inner  $4$  arcsec  $\times$   $4$  arcsec is suspicious. Deeper and/or higher frequency observations will be needed to definitively understand the diverse continuum emission from NGC 404.

## 5.3 Intermediate-mass black hole

Our modelling reveals the presence of a dark object in NGC 404, of a mass of  $\approx 5 \times 10^5 M_\odot$ , this from both stellar kinematic and molecular gas kinematic modelling. The radius of the sphere-of-influence of this BH ( $R_{\text{SOI}}$ ) can be calculated using the standard equation

$$R_{\text{SOI}} = \frac{GM_{\text{BH}}}{\sigma_e^2}, \quad (2)$$

where  $G$  is the gravitational constant and  $\sigma_e$  the stellar velocity dispersion. In NGC 404 this equates to  $0.''1$  (or  $\approx 1.4$  pc). This  $R_{\text{SOI}}$  is of similar size to the point-spread function of our op-

tical data ( $\approx 0.''12$ ), and is well resolved by our high-resolution molecular gas data with a synthesized beam of  $0.''051 \times 0.''026$  (or  $\approx 0.54$  pc<sup>2</sup>).

Crucially, to bring our stellar and molecular gas measurements into agreement we needed to include the contribution of the molecular gas to the gravitational potential of this object. While the molecular material does not dominate the potential at any radius, it does provide a significant contribution towards the outer edge of the central molecular disc (see Fig. 9). Including its effect decreases the derived mass mismatch factor ( $\Gamma$ ), and increases the black hole mass required compared to the analysis in Nguyen et al. (2017), bringing these two measurements into agreement. It also brings the stellar kinematic measurement into better agreement with the hot-H<sub>2</sub> kinematic measurement of Nguyen et al. (2017). This highlights the need to accurately determine the mass and distribution of molecular material around intermediate-mass BHs when attempting to measure their mass, even when using stellar kinematics.

In Fig. 13 we show our measurement of the BH mass in NGC 404 as a blue data point on the  $M_{\text{BH}}-\sigma_e$  relations of van den Bosch (2016), Greene et al. (2019), and on the  $M_{\text{BH}}-\text{bulge mass}$  ( $M_{\text{bulge}}$ ) relation of McConnell & Ma (2013). We highlight other measurements using the molecular gas technique with red data points. Bulge masses for objects with molecular gas estimated BH masses are taken from McConnell & Ma (2013), Krajnović et al. (2013), Salo et al. (2015), and Savorgnan & Graham (2016), while velocity dispersions are as quoted in the mass measurement papers. The mass of the IMBH in NGC 404 agrees reasonably well with the extrapolations of the relations presented in these works, being slightly above the  $M_{\text{BH}}-\sigma_e$  and slightly below the  $M_{\text{BH}}-M_{\text{bulge}}$  relation. Obtaining more measurements of low-mass BHs is clearly crucial to better anchor these relations.

#### 5.4 Stellar mass normalization

Our kinematic modelling uses a model of the stellar mass of NGC 404 created from *HST* photometry using pixel-by-pixel colour to mass-to-light ratio relations, carefully normalized using stellar population estimates of the mass-to-light ratios based on Space Telescope Imaging Spectrograph (STIS) spectra assuming a Chabrier (2003) IMF. As such, this model should provide an excellent measurement of the stellar contribution to the potential.

Here we also included in the fit a stellar mass normalization factor, that should be approximately unity assuming no systematic effect is present. However, as shown above, our stellar kinematic modelling requires a significantly lower stellar mass normalization ( $\Gamma \approx 0.6$ ). This suggests the stellar population is significantly less massive than expected assuming a Chabrier (2003) IMF.

The cause of this change is difficult to establish. One possibility is that the IMF of NGC 404 is significantly lighter than assumed. Significant variations have been observed in the IMFs of massive early-type galaxies (see e.g. van Dokkum & Conroy 2010; Cappellari et al. 2012; Martín-Navarro et al. 2015), and the extrapolations of at least some of the trends reported in the literature would support the idea of a lower IMF normalization in this dwarf elliptical galaxy. For instance, some authors (e.g. Cappellari et al. 2012) suggest that the velocity dispersion of an ETG is the best predictor of its IMF. Fig. 14 shows the IMF measurements from that work (as tabulated in Cappellari et al. 2013b) and those of Davis & McDermid (2017) and Nguyen et al. (2019), plotted against stellar velocity dispersions measured within the same apertures. Shown in blue is our estimate of the IMF mismatch parameter  $\alpha_{\text{IMF}}$  in NGC 404, which is our stellar

mass normalization factor  $\Gamma$  re-normalized to a Salpeter (1955) IMF via  $\alpha_{\text{IMF}} = 0.58 \Gamma$  (where this proportionality constant comes from ratio of the integral of these IMFs). While the  $\alpha_{\text{IMF}}$  values derived here (and those of Nguyen et al. 2019) are only valid for the nuclear star clusters of their parent galaxy (rather than for the entire galaxy), our measurement for NGC 404 is consistent with the extrapolation of the best-fitting relation of Cappellari et al. (2012, 2013a). Interestingly, NGC 404 has a high metallicity and thus, if real, the low stellar-mass normalization of NGC 404 would be less consistent with metallicity–IMF relations (e.g. from Martín-Navarro et al. 2015). This suggests that further work on the IMF properties of dwarf elliptical galaxies could help shed light on the drivers of IMF variations in the early-type galaxy population (see e.g. Mentz et al. 2016).

Having said that, a changing IMF is not the only possible explanation of our low derived  $\Gamma$ . Another possibility is that the star formation history (SFH) of NGC 404 has not been correctly estimated by Nguyen et al. (2017), who used a non-parametric approach fitting combinations of models with ages of 1, 10, 50, 100, 300, 600, 1000, 2500, 5000, 10 000, and 13 000 Myr. The low  $\Gamma$  obtained here could be explained if the best SFH fit has too many old stars (or not enough young stars). Nguyen et al. (2017) found an unusual stellar population in the nucleus, with a dominant 1 Gyr old population. This is an age where asymptotic giant branch stars contribute significantly to the luminosity, and it is possible these are not accurately modelled (which could result in a mis-estimation of the SFH). We note that in the nuclear star clusters of three other galaxies studied by Nguyen et al. (2019) (and shown in orange in Fig. 14) without significant molecular gas (and thus star formation), the  $\Gamma$  values are all consistent with a Chabrier IMF, albeit with relatively large uncertainties. Yet another possibility is that we have overestimated the mass of gas present in the nucleus of NGC 404 (e.g. by assuming an incorrect  $\alpha_{\text{CO}}$ ). Despite the differing sensitivities of our stellar and gas BH mass measurement to this quantity (see Section 4.5), this possibility cannot be ruled out using our current data alone. We therefore suggest that the low  $\Gamma$  value should be treated with caution.

## 6 CONCLUSIONS

In this work we presented observations of the molecular ISM in the dwarf elliptical galaxy NGC 404 at an unprecedented linear resolution of  $\approx 0.5$  pc. We used these observations, in conjunction with Gemini observations of the stellar kinematics, to estimate the mass of the intermediate-mass black hole at the heart of this object.

Our ALMA observations revealed a central disc/torus of molecular gas which peaks in surface density at a radius of  $\approx 0.''16$  (2.3 pc) and has an exponential scale-height smaller than 1.3 pc. This disc is inclined to the line of sight and is clearly rotating around the IMBH. It is surrounded by a kinematically distinct lopsided arm/spiral feature, connecting to a nearly face-on incomplete (pseudo)-ring of emission with a radius of  $2.''7$  ( $\approx 40$  pc). Scattered molecular clouds also exist beyond this radius.

Continuum emission is detected from the central parts of NGC 404 (tracing the central disc and lopsided arm) and from several other locations at larger radii. The extended central continuum source is likely dominated by dust continuum emission, with possible small contributions from synchrotron emission from the small jet in the centre, and hydrodynamic shocks along the arm. The outer sources could be the most extreme molecular star-forming clumps in this object or an overdensity of background galaxies.

By combining the molecular gas data with constraints on galaxy parameters from stellar kinematic modelling we were able to con-

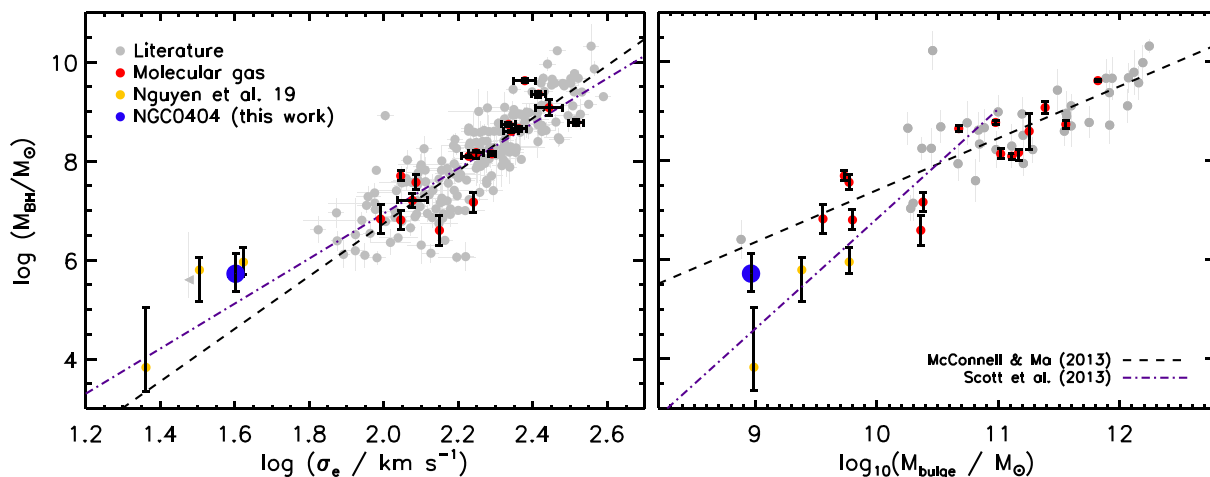


**Figure 13.** Left-hand panel:  $M_{\text{BH}}-\sigma_e$  relation (grey data points and black dashed line) from the compilation of van den Bosch (2016). We show the BH mass measured for NGC 404 here as a large blue data point, and highlight other measurements using the molecular gas technique with red data points (Davis et al. 2013b; Onishi et al. 2015; Barth et al. 2016a,b; Davis et al. 2017, 2018; Onishi et al. 2017; Boizelle et al. 2019; Combes et al. 2019; Nagai et al. 2019; North et al. 2019; Smith et al. 2019; Nguyen et al. 2020). In yellow we show the BH masses of low-mass galaxies measured in Nguyen et al. (2019). We also show the best fitting relation (for all galaxies, including upper limits in the IMBH regime) from Greene et al. (2019) as a purple dot-dashed line. Right-hand panel:  $M_{\text{BH}}-M_{\text{bulge}}$  relation from the compilation of McConnell & Ma (2013) (black dashed line) and Scott, Graham & Schombert (2013) (purple dot-dashed line). Symbols are as in the left figure. Bulge masses for objects with molecular gas-estimated BH masses are taken from McConnell & Ma (2013), Krajnović et al. (2013), Salo et al. (2015), and Savorgnan & Graham (2016). In both panels, our measurement of the BH mass of NGC 404 is reasonably consistent with the best-fitting relation(s).

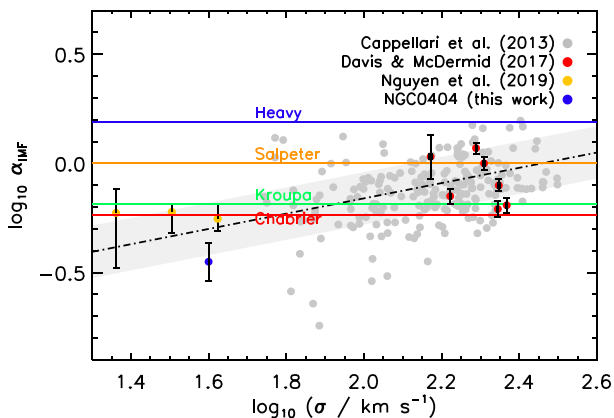


**Figure 14.** The IMF mismatch parameter ( $\alpha_{\text{IMF}}$ ) plotted against the stellar velocity dispersion ( $\sigma$ ) measured within the same aperture. Our measurement in NGC 404 is shown in blue, while measurements from Cappellari et al. (2012), Davis & McDermid (2017), and Nguyen et al. (2019) are shown in grey, red, and orange, respectively. Also shown are solid coloured lines that denote the  $\alpha_{\text{IMF}}$  parameter of a heavy, Salpeter, Kroupa, and Chabrier IMF. A black dot-dashed line denotes the best fit correlation of Cappellari et al. (2012, 2013a), and the grey shaded region around it denotes the reported scatter around that relation of 0.12 dex. Our estimate of the IMF mismatch in NGC 404 is marginally consistent with the extrapolation of the best-fitting relation.

strain the mass of the IMBH in NGC 404 using two independent techniques. We showed here that, once we include the contribution of the molecular gas to the gravitational potential, the observed stellar kinematics require a black hole mass of  $5.1^{+14}_{-4.5} \times 10^5 M_{\odot}$  (at the 99 per cent CL). We were also able to estimate the mass of the IMBH in NGC 404 directly from the molecular gas kinematics, utilizing a forward modelling approach in a Bayesian framework

to fit the observed data cube. We again clearly detect the presence of a dark object, with a mass of  $5.5^{+4.1}_{-3.8} \times 10^5 M_{\odot}$  (again at the 99 per cent CL), in good agreement with our stellar kinematic measurement. In both cases the BH mass inferred is larger than that previously estimated using the stellar kinematics alone. This is because the molecular material in this object contributes non-negligibly to the potential, systematically biasing the determination of the BH mass. This highlights the need to accurately determine the mass and distribution of all dynamically important components around low-mass BH's when attempting to measure their mass.

Our derived black hole mass for NGC 404 is broadly consistent with extrapolations from the  $M_{\text{BH}}-\sigma_e$  and  $M_{\text{BH}}-M_{\text{bulge}}$  relations. Drawing strong conclusions about the distribution of IMBH masses and how they correlate with galaxy properties will, however, require larger samples. ALMA is poised to contribute significantly to this, both through providing maps of the dynamically important molecular material, and by directly tracing its rotation around the black holes themselves.

## ACKNOWLEDGEMENTS

TAD acknowledges support from a Science and Technology Facilities Council Ernest Rutherford Fellowship and through grant ST/S00033X/1. TAD thanks Michael Anderson, Mattia Negrello, Andrew Rigby, and Elizabeth Watkins for helpful discussions, and the anonymous referee whose suggestions improved this paper. Research by ACS is supported by National Science Foundation (NSF) grant AST-1350389. Basic research in radio astronomy at the U.S. Naval Research Laboratory is supported by 6.1 Base Funding. MB was supported by the consolidated grants ‘Astrophysics at Oxford’ ST/N000919/1 and ST/K00106X/1 from the UK Research Council. Research by AJB is supported by NSF grant AST-1614212. TGW acknowledges funding from the European Research Council

(ERC) under the European Union’s Horizon 2020 research and innovation programme (grant agreement No. 694343).

This paper makes use of the following ALMA data:

- (i) ADS/JAO.ALMA#2015.1.00597.S
- (ii) ADS/JAO.ALMA#2017.1.00572.S
- (iii) ADS/JAO.ALMA#2017.1.00907.S

ALMA is a partnership of ESO (representing its member states), NSF (USA) and NINS (Japan), together with NRC (Canada), MOST and ASIAA (Taiwan), and KASI (Republic of Korea), in cooperation with the Republic of Chile. The Joint ALMA Observatory is operated by ESO, AUI/NRAO, and NAOJ. The National Radio Astronomy Observatory is a facility of the National Science Foundation operated under cooperative agreement by Associated Universities, Inc.

This paper is also based, in part, on observations made with the NASA/ESA *Hubble Space Telescope*, and obtained from the Hubble Legacy Archive, which is a collaboration between the Space Telescope Science Institute (STScI/NASA), the Space Telescope European Coordinating Facility (ST-ECF/ESA), and the Canadian Astronomy Data Centre (CAD/C/NRC/CSA).

## REFERENCES

- Andrae R., 2010, preprint ([arXiv:1009.2755](https://arxiv.org/abs/1009.2755))
- Barth A. J., Boizelle B. D., Darling J., Baker A. J., Buote D. A., Ho L. C., Walsh J. L., 2016a, *ApJ*, 822, L28
- Barth A. J., Darling J., Baker A. J., Boizelle B. D., Buote D. A., Ho L. C., Walsh J. L., 2016b, *ApJ*, 823, 51
- Boehle A., Larkin J. E., Armus L., Wright S. A., 2018, *ApJ*, 866, 79
- Boizelle B. D., Barth A. J., Walsh J. L., Buote D. A., Baker A. J., Darling J., Ho L. C., 2019, *ApJ*, 881, 10
- Bresolin F., 2013, *ApJ*, 772, L23
- Cai Z.-Y. et al., 2013, *ApJ*, 768, 21
- Cappellari M. et al., 2012, *Nature*, 484, 485
- Cappellari M. et al., 2013a, *MNRAS*, 432, 1709
- Cappellari M. et al., 2013b, *MNRAS*, 432, 1862
- Cappellari M., 2002, *MNRAS*, 333, 400
- Cappellari M., 2008, *MNRAS*, 390, 71
- Chabrier G., 2003, *PASP*, 115, 763
- Coccolato L., Sarzi M., Pizzella A., Corsini E. M., Dalla Bontà E., Bertola F., 2006, *MNRAS*, 366, 1050
- Combes F. et al., 2019, *A&A*, 623, A79
- Dame T. M., 2011, preprint ([arXiv:1101.1499](https://arxiv.org/abs/1101.1499))
- Davis T. A. et al., 2013a, *MNRAS*, 429, 534
- Davis T. A. et al., 2018, *MNRAS*, 473, 3818
- Davis T. A., McDermid R. M., 2017, *MNRAS*, 464, 453
- Davis T. A., Bureau M., Cappellari M., Sarzi M., Blitz L., 2013b, *Nature*, 494, 328
- Davis T. A., Bureau M., Onishi K., Cappellari M., Iguchi S., Sarzi M., 2017, *MNRAS*, 468, 4675
- del Río M. S., Brinks E., Cepa J., 2004, *AJ*, 128, 89
- den Brok M. et al., 2015, *ApJ*, 809, 101
- Dickman R. L., Snell R. L., Schloerb F. P., 1986, *ApJ*, 309, 326
- Dumont A., Seth A. C., Strader J., Greene J. E., Burtscher L., Neumayer N., 2020, *ApJ*, 888, 19
- Emsellem E., Monnet G., Bacon R., Nieto J. L., 1994, *A&A*, 285, 739
- Gebhardt K. et al., 2001, *AJ*, 122, 2469
- Greene J. E., 2012, *Nat. Commun.*, 3, 1304
- Greene J. E., Ho L. C., Barth A. J., 2008, *ApJ*, 688, 159
- Greene J. E., Strader J., Ho L. C., 2019, *ARA&A*, preprint ([arXiv:1911.09678](https://arxiv.org/abs/1911.09678))
- Inayoshi K., Visbal E., Haiman Z., 2020, *ARA&A*, 58, 1
- Karachentsev I. D. et al., 2002, *A&A*, 389, 812
- Kormendy J., Ho L. C., 2013, *ARA&A*, 51, 511
- Krajnović D. et al., 2013, *MNRAS*, 432, 1768

- Lelli F., McGaugh S. S., Schombert J. M., Pawlowski M. S., 2016, *ApJ*, 827, L19
- Leroy A. K. et al., 2009, *AJ*, 137, 4670
- Madau P., Rees M. J., 2001, *ApJ*, 551, L27
- Martín-Navarro I. et al., 2015, *ApJ*, 806, L31
- McConnell N. J., Ma C.-P., 2013, *ApJ*, 764, 184
- McKee C. F., Hollenbach D. J., 1987, *ApJ*, 322, 275
- Medling A. M. et al., 2019, *ApJ*, 885, L21
- Mentz J. J. et al., 2016, *MNRAS*, 463, 2819
- Miller B. P., Gallo E., Greene J. E., Kelly B. C., Treu T., Woo J.-H., Baldassare V., 2015, *ApJ*, 799, 98
- Mitzkus M., Cappellari M., Walcher C. J., 2017, *MNRAS*, 464, 4789
- Molinari S. et al., 2011, *ApJ*, 735, L33
- Nagai H. et al., 2019, *ApJ*, 883, 193
- Nguyen D. D. et al., 2017, *ApJ*, 836, 237
- Nguyen D. D. et al., 2018, *ApJ*, 858, 118
- Nguyen D. D. et al., 2019, *ApJ*, 872, 104
- Nguyen D. D. et al., 2020, *ApJ*, 892, 68
- North E. V. et al., 2019, *MNRAS*, 490, 319
- Nyland K. et al., 2017, *ApJ*, 845, 50
- Onishi K., Iguchi S., Sheth K., Kohno K., 2015, *ApJ*, 806, 39
- Onishi K., Iguchi S., Davis T. A., Bureau M., Cappellari M., Sarzi M., Blitz L., 2017, *MNRAS*, 468, 4663
- Rau U., Cornwell T. J., 2011, *A&A*, 532, A71
- Reines A. E., Greene J. E., Geha M., 2013, *ApJ*, 775, 116
- Ricarte A., Natarajan P., 2018, *MNRAS*, 481, 3278
- Salo H. et al., 2015, *ApJS*, 219, 4
- Salpeter E. E., 1955, *ApJ*, 121, 161
- Savorgnan G. A. D., Graham A. W., 2016, *MNRAS*, 457, 320
- Scott N., Graham A. W., Schombert J., 2013, *ApJ*, 768, 76
- Seth A. C. et al., 2010, *ApJ*, 714, 713
- Shu F. H., 1992, *The Physics of Astrophysics. Volume II: Gas Dynamics.* University Science Books, Mill Valley, CA ISBN 0-935702-65-2
- Smith M. D. et al., 2019, *MNRAS*, 485, 4359
- Spitzer Lyman J., 1942, *ApJ*, 95, 329
- Taylor C. L., Petitpas G. R., del Río M. S., 2015, *AJ*, 149, 187
- Thilker D. A. et al., 2010, *ApJ*, 714, L171
- Urquhart J. S. et al., 2018, *MNRAS*, 473, 1059
- Valluri M., Ferrarese L., Merritt D., Joseph C. L., 2005, *ApJ*, 628, 137
- van den Bosch R. C. E., 2016, *ApJ*, 831, 134
- van den Bosch R. C. E., van de Ven G., 2009, *MNRAS*, 398, 1117
- van Dokkum P. G., Conroy C., 2010, *Nature*, 468, 940
- Volonteri M., 2012, *Science*, 337, 544
- Volonteri M., Haardt F., Madau P., 2003, *ApJ*, 582, 559

## APPENDIX A: MOLECULAR GAS KINEMATIC FITTING INCLUDING DISC THICKNESS

As discussed in Section 4.5 we are able to adapt our fitting procedure to study the effect of the assumed thickness of the molecular gas disc/torus in the centre of NGC 404. We add a free parameter for the disc thickness (denoted  $z_h$ ) to the model described in Section 4, which we assume is radially constant. The molecular ‘cloudlets’ that make up our SKYSAMPLER model are given randomly allocated offsets in the  $z$ -direction drawn from a Gaussian distribution centred around zero, and with a standard deviation of  $z_h$ . This 3D distribution of gas cloudlets is then input to the KINMS simulation routines, which calculate the potential of the resulting molecular gas distribution, and create mock observations which can be directly compared to the data as part of our MCMC fitting procedure.

The results of this analysis are shown in Fig. A1. We obtain an upper limit on the scale-height  $z_h$  itself, constraining  $z_h < 1.3$  pc at the  $1\sigma$  confidence level. While the BH mass we derive does have a dependence on  $z_h$  (with thicker discs requiring a larger best-fitting BH mass), this change is not significant within the uncertainties. We

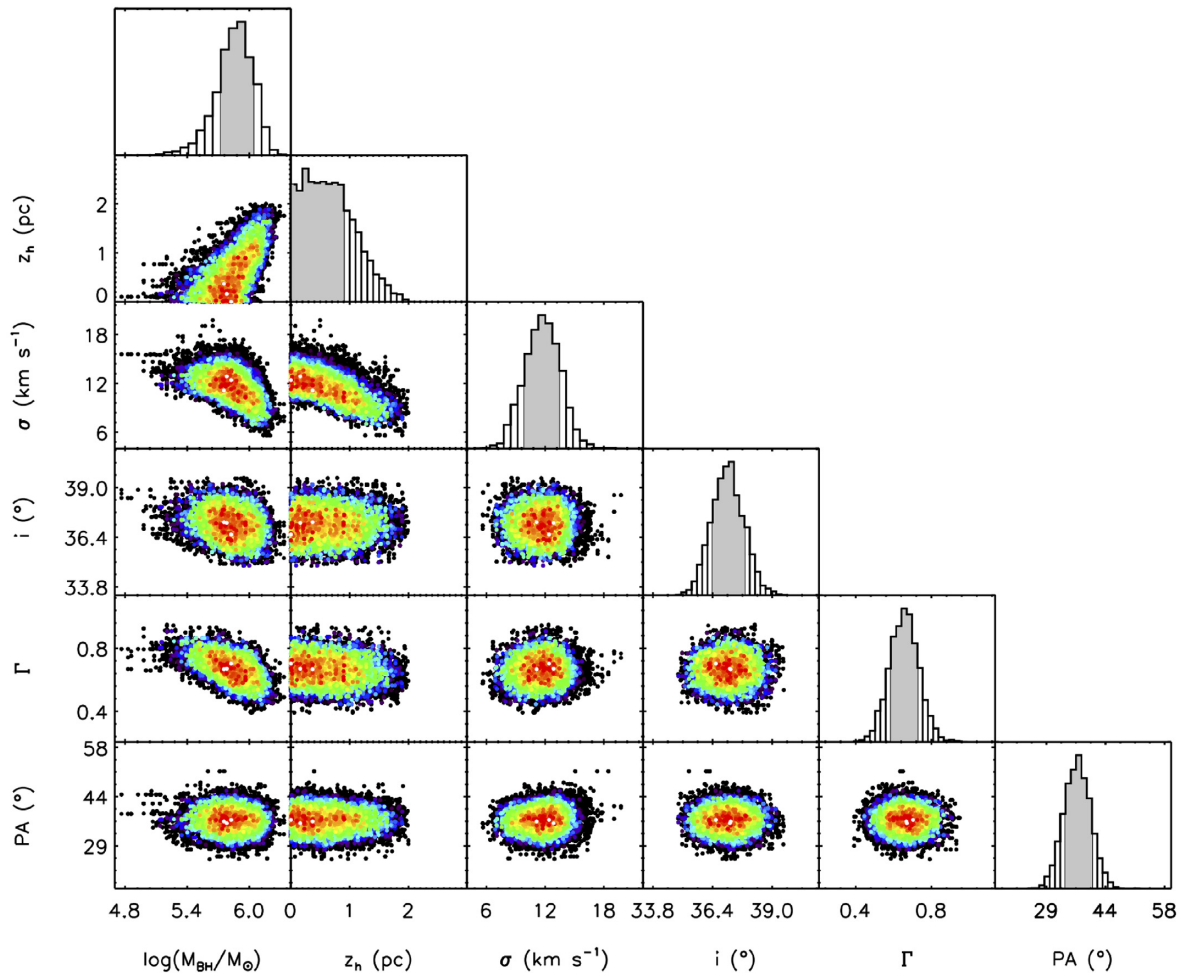


**Figure A1.** Results of kinematic fitting to the molecular gas in NGC 404, as Fig. 10, but including the effect of disc thickness ( $z_h$ ). Assuming the molecular gas disc/torus in the central parts of this object (with a radius  $r = 3.7$  pc) is geometrically thick does not change our best-fitting BH mass significantly. We are, however, able to set a  $1\sigma$  limit to the vertical scale-height of  $z_h < 1.3$  pc.

thus do not expect the thickness of the molecular torus in this object to be significantly affecting the main results of this paper.

The limit we derive for the molecular scale-height in NGC 404 is fully consistent with expectations from simple theoretical models. Following Shu (1992), the vertical gas density profile in a non-self-gravitating gas disc rotating in a spherically symmetric potential will have a Gaussian form at any radius  $r$  (consistent with the assumption made for the vertical distribution in our modelling), where the scale height  $z_h$  is given by

$$z_h = \sqrt{2} \left( \frac{\sigma_z}{V_\phi} \right) r, \quad (\text{A1})$$

where  $\sigma_z$  is the gas velocity dispersion in the vertical direction and  $V_\phi$  is the component of the velocity in the azimuthal direction. As described above  $V_\phi/\sigma_z \gtrsim 5$  everywhere in the central regions of NGC 404, and thus at the outer edge of the molecular disc/torus we would predict  $z_h \lesssim 0.8$  pc, consistent with our derived upper limit.

Alternatively one can consider the case of a disc dominated by its own self-gravity, where the vertical scale height is given by

$$z_h = \frac{\sigma_z^2}{\pi G \Sigma_{\text{gas}}}, \quad (\text{A2})$$

where  $\Sigma_{\text{gas}}$  is the gas surface density (Spitzer 1942). Inputting the measured values of these quantities for NGC 404 ( $\Sigma_{\text{gas}} \approx 10\,000 M_\odot \text{pc}^{-2}$ ,  $\sigma_z = 12.9 \text{ km s}^{-1}$ ) gives an estimate of  $z_h = 1.2$  pc, again consistent with our derived upper limit. We note that the vertical gas density distribution in this case should have a  $\text{sech}^2(z)$  form, and thus this scale-height is not directly comparable with that derived above. Their similarity does, however, suggest our upper limit to the scale-height of the disc/torus in NGC 404 is reasonable.

<sup>1</sup>*School of Physics and Astronomy, Cardiff University, Queens Buildings, The Parade, Cardiff CF24 3AA, UK*

<sup>2</sup>*National Astronomical Observatory of Japan (NAOJ), National Institute of Natural Sciences (NINS), 2-21-1 Osawa, Mitaka, Tokyo 181-8588, Japan*

<sup>3</sup>*Department of Physics and Astronomy, University of Utah, 115 South 1400 East, Salt Lake City, UT 84112, USA*

<sup>4</sup>*Department of Astrophysics, Princeton University, Princeton, NJ 08544, USA*

<sup>5</sup>*National Research Council, Resident at the U.S. Naval Research Laboratory, 4555 Overlook Ave SW, Washington, DC 20375, USA*

<sup>6</sup>*Department of Physics and Astronomy, University of California, Irvine, 4129 Frederick Reines Hall, Irvine, CA 92697, USA*

<sup>7</sup>*Sub-Department of Astrophysics, Department of Physics, University of Oxford, Denys Wilkinson Building, Keble Road, Oxford OX1 3RH, UK*

<sup>8</sup>*Yonsei Frontier Lab and Department of Astronomy, Yonsei University, 50 Yonsei-ro, Seodaemun-gu, Seoul 03722, Republic of Korea*

<sup>9</sup>*Leibniz-Institut für Astrophysik Potsdam (AIP), An der Sternwarte 16, D-14482 Potsdam, Germany*

<sup>10</sup>*Department of Astronomical Science, SOKENDAI (The Graduate University of Advanced Studies), Mitaka, Tokyo 181-8588, Japan*

<sup>11</sup>*Max-Planck-Institut für Astronomie, Königstuhl 17, D-69117 Heidelberg, Germany*

<sup>12</sup>*Department of Space, Earth and Environment, Chalmers University of Technology, Onsala Observatory, SE-439 92 Onsala, Sweden*

<sup>13</sup>*Armagh Observatory and Planetarium, College Hill, Armagh BT61 9DG, UK*

This paper has been typeset from a  $\text{\TeX}/\text{\LaTeX}$  file prepared by the author.